Spring 2020

Auto-stratigraphic evolution of experimental crater-fill basins: Implications for interpreting Mars sequence stratigraphy and paleoclimate

Lexie Stodden
Western Washington University, lexstod@gmail.com

Auto-stratigraphic evolution of experimental crater-fill basins: Implications for interpreting Mars sequence stratigraphy and paleoclimate

By

Lexie Stodden

Accepted in Partial Completion
of the Requirements for the Degree
Master of Science

ADVISORY COMMITTEE

Dr. Brady Foreman, Chair

Dr. Melissa Rice

Dr. Robert Mitchell

Dr. Robyn Dahl

GRADUATE SCHOOL

David L. Patrick, Interim Dean

Master's Thesis

In presenting this thesis in partial fulfillment of the requirements for a master's degree at Western Washington University, I grant to Western Washington University the non-exclusive royalty-free right to archive, reproduce, distribute, and display the thesis in any and all forms, including electronic format, via any digital library mechanisms maintained by WWU.

I represent and warrant this is my original work and does not infringe or violate any rights of others. I warrant that I have obtained written permissions from the owner of any third party copyrighted material included in these files.

I acknowledge that I retain ownership rights to the copyright of this work, including but not limited to the right to use all or part of this work in future works, such as articles or books.

Library users are granted permission for individual, research and non-commercial reproduction of this work for educational purposes only. Any further digital posting of this document requires specific permission from the author.

Any copying or publication of this thesis for commercial purposes, or for financial gain, is not allowed without my written permission.

Lexie Stodden

May 20th, 2020

This thesis uses the plural first-person pronouns as it will be admitted for publication with multiple authors.

Auto-stratigraphic evolution of experimental crater-fill basins: Implications for interpreting Mars sequence stratigraphy and paleoclimate

A Thesis
Presented to
The Faculty of
Western Washington University

In Partial Fulfillment
Of the Requirements for the Degree
Master of Science

by
Lexie Stodden
May 2020

Abstract

Preserved fluvial and deltaic sedimentary deposits found within martian crater-fill basins are important evidence documenting past warmer, wetter climatic periods on Mars. The morphologic and stratigraphic patterns of these sedimentary deposits are commonly interpreted to record variably complex transgression and regression histories of crater-lake levels, driven by fluctuations in the prevailing hydroclimatic conditions. Yet this tendency for direct inversion of sedimentary characteristics to formative boundary conditions largely neglects large-scale autogenic processes operating in crater-fill basins. The goal of this research is to illustrate an idiosyncratic feature of these basin types, wherein attributes of the sediment source play an outsized role in dictating conditions of the sink that ultimately stores the sediment. This linkage is rarely a concern in sedimentary basins on Earth but appears to strongly influence martian stratigraphy. Here, we examine sequence stratigraphic patterns produced in an experimental sedimentary basin wherein an initially empty basin passively receives a constant sediment flux and water discharge until reaching a spill-point elevation. This experimental setup captures the simplest of all feasible crater-fill basin evolution histories, and we present data from five experiments that vary the initial basin size and sediment flux parameters. We used Computed Tomography (CT) scans to analyze internal deltaic stratigraphy and found that five main sequence stratigraphic phases are produced. These phases are spontaneously generated under constant boundary conditions, indicating they are autogenic and directly attributable to the consequences of mass balance. As sediment and water input volumes "compete" for accommodation in the crater they cause five major depositional phases: 1) an early fluvial progradational phase; 2) a transitional phase from fluvial to deltaic progradational deposition; 3) a retreat phase of retrogradation/aggradational back-stepping deltaic deposition; 4) an over-topping phase of late progradational delta deposition; and 5) a forced progradational phase when steady state base level is reached. This experimental sequence stratigraphic pattern compares favorably with well-studied martian crater-fill sedimentary packages such as the Eberswalde Delta, the Southwest Eberswalde Deposit and the Jezero Western Delta. Thus, we suggest our experiments constitute a alternative, but useful "starting" sequence stratigraphic framework for approaching crater-fills rather than a direct application of marine sequence stratigraphic models, which assume an infinitely large ocean basin.

Acknowledgements

This research was possible due to the funding provided by the ACS-Petroleum Research Fund Undergraduate New Investigator Grant (#57156 UNI-8) to B.Z.F. and M.D.D. As well as Western Washington University Geology department and the Western Washington University Graduate School.

I wish to thank all the people who helped me accomplish this research project. Thank you for helping me build, run, fix and transport my experiments: Ben Paulson, Jim Mullen, Grace Sutherland, Jessica Welch, Anna Schluneger, Bo Ward, Zach Leija, Ya-Li Lizik, Ariana Flournoy, Emma Sullivan, and Olivia Eggert & Tuba. I could not have accomplished this work without you all.

Thank you to my thesis committee for the taking the time to provide valuable insight on how to become a better writer and researcher: Melissa Rice, Bob Mitchell, Robyn Dahl and Mike D'Emic.

Thank you to my cohort and the entire WWU Geology Department for welcoming a New Yorker with open arms into the beautiful PNW geology community.

Thank you to my parents and my brother for your endless love and support.

Thank you to all the amazing friends I was lucky enough to gain along the way. I am so happy to have made such meaningful and long-lasting connections with you all. I feel so fortunate to know I have such a big Bellingham family.

Finally, thank you to Brady Foreman. None of this would have been possible if you had not believed in me, guided me and supported me through all the (many) ups and downs this graduate degree threw at us. You are an outstanding advisor and an exceptional person. I am so proud to have been your graduate student.

"Individually we are one drop. Together we are an ocean."

-Ryunosuke Satoro

Table of Contents

List of Tables and Figures

1. Introduction

1.1. Mars climate and stratigraphy

Modern Mars is a planet with surface temperatures and pressures that cannot support water in its stable liquid state (e.g., Ingersoll, 1970; Haberle et al., 2001; Martinez and Renno, 2013). Water does exist stably as extensive ice sheets covering large portions of the martian surface and subsurface, and in trace concentrations in its vapor state within the martian atmosphere (e.g., Forget, 2009; Martinez et al., 2017). However, this has not always been the case throughout Mars' planetary history. Geomorphic and stratigraphic features provide clear evidence that during the planet's early history, particularly the Early Noachian to the Early Hesperian (3.9 – 3.6 Ga), the climatic conditions were able to support large amounts of liquid water (e.g., Malin and Edgett, 1999; 2003; Forget, 2009; Kite et al., 2019). Water-related geomorphic features include lacustrine, fluvial, and deltaic deposits on Mars (e.g., Malin and Edgett, 2000; Moore et al., 2003; Pondrelli et al., 2008). Many of these water-related sedimentary deposits are found within impact craters, which allowed the accumulation of thick stratigraphic successions that preserve a history of sediment transport processes.

Despite clear evidence for the presence of water, there has been widespread disagreement and uncertainty in the estimates of the time duration and persistence of liquid water on Mars. Broadly speaking, two endmember hypotheses have been discussed extensively in the literature. The long-term hydrologic hypothesis suggests wet climatic periods lasting millions of years (e.g., Craddock and Howard, 2002; Andrews-Hannah and Lewis, 2011; Kite et al., 2012; Kite et al., 2019), whereas the short-term hydrologic hypothesis argues that fluid flow and the development of the associated geomorphic features occurred over time scales less than 100 years (e.g., Jerolmack et al., 2004; Irwin et al., 2015) to a maximum of ~10,000 years (Bhattacharya et al., 2005). For example, the Eberswalde Delta located within the western basin of the Eberswalde Crater, formerly known as the Holden NE Crater, has been interpreted as being generated by both short-lived flashy depositional events and long-lived persistent flow conditions (Jerolmack et al., 2004; Bhattacharya et al., 2005; Lewis and Aharonson, 2006; Pondrelli et al., 2008; Irwin et al., 2015). Resolving these two endmember scenarios relies heavily on the accuracy of interpreted stratigraphic sequences and depositional patterns, such as thickness, volume, areal extent, and internal sedimentologic features of sedimentary crater-fills.

Some researchers have taken reconstructions of the martian hydroclimate one step further by applying sequence stratigraphic and cyclostratigraphic techniques to crater-fill sedimentary successions. Sequence stratigraphic interpretations infer lake-level history, and by extension, climate, from progradational, aggradational, and retrogradational stacking patterns of fluvio-deltaic strata within crater-fills (Bhattacharya et al., 2005; Pondrelli et al., 2008; Goudge et al., 2018). These stacking patterns broadly track shoreline positions through time, and putatively relate to meteoric/fluvial water input to the crater and evaporative/infiltration output of water (Mangold et al., 2012). Other studies have performed time series analyses on bed thickness patterns in martian crater-fills, a technique applied to some Earth sedimentary sequences (Olsen, 1990; Olsen & Kent, 1999; Schwarzacher, 2000). From sedimentary bedding cycles these studies hypothesize that insolation-driven, Milankovitch-scale climate variations ("wet" and "dry" oscillations) controlled lacustrine base level within martian lakes (Lewis et al., 2008, 2010). Again, these hydroclimate hypotheses and interpretations rest on accurately inverting stratigraphic patterns into the driving boundary conditions. This makes a comprehensive understanding of crater-fill basin evolution necessary to have confidence in the interpreted hydroclimate fluctuations.

1.2. Allogenic and autogenic stratigraphy

On Earth stratigraphic patterns are commonly interpreted as being driven by a combination of allogenic (i.e., external) and autogenic (i.e., internal) processes. Climate, tectonics, and eustasy are viewed at the major allogenic boundary conditions that drive the production, transport, and generation of accommodation space that allows long-term storage of sediment (Watts, 1982; Posamentier et al., 1988; Schlager, 1993; Paola, 2000; Paola and Voller, 2005). Yet allogenic forcings may produce similar depositional products to one another, a phenomenon known as convergence (Schumm and Lichty, 1965). For example, in the case of fluvio-deltaic settings, tectonic uplift events or climate change may produce an increase in sediment supply that leads to progradational stratigraphic patterns within a basin, but a sea-level fall can also produce a similar progradational patterns (Postma, 1990; Heijst and Postma, 2001; Gobo et al., 2014; 2015). Alternatively, a reduction in sediment supply via tectonic quiescence or climate change may produce retrogradational stratigraphic patterns, a pattern also possibly induced by eustatic sea-level rise (Postma et al., 2008). Tectonic subsidence and sediment compaction within the basin itself further complicate reconstructing allogenic forcings from stratigraphy since these factors create additional accommodation for sediment beyond eustatic fluctuations. On Earth there are a

suite of geochemical and paleobiologic proxies, provenance indicators, and chronostratigraphic constraints that aid in discriminating amongst allogenic forcings (Paola et al., 1992; Duller et al., 2010; Armitage et al., 2011; Hampson et al., 2014; Toby et al., 2019). However, these are currently unavailable for martian systems.

In the broadest sense allogenic forcings result in significant basinward or landward shifts in depositional environments in deltaic systems, most notably the position of the shoreline (Kim et al., 2006a, 2006b; Jerolmack, 2009). The physical scales of these stratigraphic shifts have commonly been thought to correlate to the magnitude and, in some cases, duration of allogenic change (Vail and Mitchum, 1979; Mitchum and Van Wagoner, 1991; Murray et al., 2017). However, beyond largely qualitative estimates there is only marginal consensus within the literature for how to recover quantitative allogenic conditions, a consensus made more tenuous by growing evidence for threshold responses and non-linearity behaviors within sedimentary systems that further complicate these endeavors (Straub et al., 2020). Furthermore, autogenic processes, those generated by internal dynamics and feedbacks within the system, overprint and add stochastic noise to the patterns driven by allogenic forcings (Karamitopoulos et al., 2014; Straub et al., 2020). Traditionally, it has been thought this autogenic variation imparted only smaller-scale variability on deposition, but recent studies indicate the scale of autogenic "noise" appears to have been underestimated during the development of sequence stratigraphic concepts and may impose deterministic stratigraphic patterns that could be confused for allogenic signals (Coe et al., 2005; Karamitopoulos et al., 2014; Hajek and Straub, 2017; Straub et al., 2020). Thus, deconvolving the myriad of boundary conditions and autogenic processes is nontrivial and requires a comprehensive assessment of basin dynamics, typically couched within a sequence stratigraphic framework.

1.3. Peculiarities of Mars basins

Martian crater-fills present a unique scenario in the context of sequence stratigraphic analysis. The initial accommodation space is generated via an extraterrestrial impact, whose size and velocity sets the volume of the depositional basin rather than tectonics as is the case on Earth (Carr et al., 1977). Furthermore, Mars is a single plate planet (e.g., Breuer and Spohn, 2003), and therefore uplift does not directly affect a crater basin and there is little reason to suspect significant tectonic subsidence nor uplift during the basin filling process (Grotzinger et al., 2011). Moreover, the basins are usually unconnected to one another and not subject to a global eustatic variation, but only the internal base-level variations of the crater lake (Cabrol and Grin, 1999). Presumably, base-

level variation is driven by the prevailing climate via precipitation-evaporation balance, infiltration into crater rock, catchment size, and topography of the crater rim (Baker et al., 1991; Craddock and Howard 2002; Mangold et al., 2004). Finally, sediment supply is not dependent on tectonic uplift events, but instead the prevailing climate, and the development of a catchment network that down-cuts into the crater wall as well as potential volcanic and/or volcaniclastic input (Pieri, 1980). In some cases, the catchment network is preserved on the modern martian surface, with its characteristics controlled by runoff, sapping, rock strength, and other parameters (Baker and Partridge, 1986; Malin and Carr, 1999; Craddock and Howard, 2002). Thus, crater-fill basins present a relatively simplistic scenario in terms of allogenic forcings as compared to Earth basins (e.g., static initial accommodation, absence of eustasy, preserved catchment structure), with climate-driven hydrologic changes being the presumptive main driver. This strengthens climate interpretations by previous studies. Yet, these idiosyncrasies of this basin type have not been explicitly examined, though they have been noted in some studies (de Villiers et al., 2013; Goudge et al., 2018).

1.4 Research Objectives

Our objective in this study is to constrain the sequence stratigraphic patterns generated by martian deltaic systems subject to invariant boundary conditions and thus generate autogenically-dominated stratigraphy. We test the hypothesis that complex aggradational, progradation, and retrogradational patterns can be generated under constant boundary conditions due to mass balance interactions using experimental basins wherein we are able to set the boundary conditions and observe the stratigraphy generated by a fluvio-deltaic system's own internal physics. This approach has been used extensively to examine basin evolution and has been successfully translated to Earth field-scale sedimentary basins (Muto and Steel, 2001a, 2001b, 2004; Paola et al., 2009). We experimentally model the simplest of all crater-fill basins possible: an initial empty "crater" volume of accommodation space filled progressively by a sediment and water volume mixture that does not change through time. Thus, all allogenic boundary conditions are constant, and the resultant stratigraphic succession driven by autogenic processes and simple mass balance requirements of a closed basin system. We assessed five combinations of initial basin volume, sediment flux, and water discharge. The experiments generated five traceable stratigraphic sequence phases: 1) early fluvial (2) mixed progradation (3) retreat (4) over-topping and (5) forced progradation. We propose that these five phases represent a baseline for martian crater-fill

stratigraphic sequence patterns, and that deviations from these patterns may be attributed to additional boundary conditions such as climatic fluctuations.

2. Experimental Background

For decades researches have used experimental methodologies to better understand fluvial and deltaic processes by constraining boundary conditions. Experiments are run on smaller spatial and shorter temporal scales than field studies, allowing more rapid testing of hypotheses in simpler systems (Muto and Steel, 2001a, 2001b, 2004; Paola et al., 2009). Moreover, experiments allow closer monitoring and more resolved data collection with explicit links to boundary conditions that drive measurable geomorphic and stratigraphic products. An added benefit of experiments is that they evolve under their own internal physics and may produce unexpected responses and behaviors not generated by numerical models wherein the physics are dictated by the researcher (Muto and Steel, 2001b; Paola et al., 2009).

Experiments can be broadly divided into two main categories, those that examine scale-dependent phenomena and those that examine scale-independent phenomena. When examining scale-dependent phenomena the researcher must appropriately “downsize” geomorphic processes in order to experimentally model them. For example, any geomorphic process that relies on fluid dynamic properties such as the Reynolds number, Froude number, or dimensionless shear stress must downscale in such a way to maintain the appropriate values. Assessing the conditions for the generation of ripples is scale-dependent on the fluid Reynolds number and sediment grain size distribution amongst other parameters (Sekiguchi and Sunamura, 2004; Ziberi et al., 2005; Pedocchi and Garcia, 2009). However, when examining scale-independent processes these experimental constraints can be relaxed. In most cases the researcher is not attempting to replicate a specific field scenario but instead capturing the overall "essence" of a geomorphic/stratigraphic problem or process. In other words, the researcher is looking for the overarching parameters or variables that are hypothesized to be the dominant influencers of the geomorphic system. For example, many attributes of "meso-scale" deltaic morphology (i.e., larger than "channel scale") such as avulsion patterns, topset and foreset geometries, gross partitioning of sediment calibers, and the mass balance interplay between sediment supply and basin accommodation all strongly appear to be scale-independent processes that can be understood through experimental

methodologies (Posamentier et al., 1992; Koss et al., 1994; Heijst and Postma, 2001; Muto and Steel, 2001a, 2001b 2004; Paola, 2009;).

Though experimental approaches are well-established for Earth-focused geomorphic/stratigraphic studies, their application by researchers to understand Mars' surface evolution is limited at present. Since the discovery and identification of preserved deltaic deposits within martian impact craters (Malin and Edgett, 2003; Moore et al., 2003; Bhattacharya et al., 2005; Lewis and Aharonson, 2006; Pondrelli et al. 2008), experiments have been used to evaluate the generative conditions of those geomorphic processes. Most pertinent to this study are those that experimentally model deltaic deposition within a closed crater basin, at least initially, during the experimental run. De Villers et al. (2013) performed several experiments that fed a constant water discharge from a pre-cut channel in a hemispherical basin carved in sand. Water discharge, "crater rim" grain size distribution, and basin hypsometry were systematically varied amongst the experiments, and the impact on delta morphology described. Sediment supply was derived from erosion of crater rim, which tended to progressively decrease over the course of the experiments. De Villers et al. (2013) identified three major phases of crater deposition, an initial phase of hyper-concentrated particle flow and water infiltration, a phase of delta back-stepping and retrogradation as the crater fills with water, and a final phase when the researchers manually breached the crater rim causing deep incision on the fan surface and the development of terraces on previous back-stepping delta deposits. The dominant influence on delta fan morphology was the increase in base level, which they ascribed to the constant input and pooling of water within the crater and the progressive reduction in sediment supply as erosion of the crater rim slowed. They also noted the influence that water discharge and grain size distribution had on the development and prevalence of depositional lobes and channelization on the delta.

Kraal et al. (2008) hypothesized that the “stair-stepping” deltaic morphology found in martian craters and described by De Villers et al. (2013) required a single, "short" duration hydrologic event as opposed to long-term continuous fluid flow or a series of discharge events. Kraal et al. (2008) also constructed a hemispherical basin, cut an initial small canyon in the crater rim, and fed a constant water discharge through this pre-constructed canyon. Initially, a debris flow dominated alluvial fan developed as water infiltrated into the permeable crater floor sediment. Subsequently, water levels rose, and a distinct deltaic system was established. Similar to De Villers et al. (2013) the back-stepping delta morphology developed. This phenomenon has been identified

in non-crater experimental basins and is caused by a base level rise that exceeds the capability of the delta to evenly distribute sediment across the entire lateral portions of the fan (Muto and Steel, 2001b). However, the internal stratigraphic products of this type of depositional pattern and phases have been unexplored, which is the focus of this study.

For martian depositional systems, both De Villers et al. (2013) and Kraal et al. (2008) found that the upstream variables (sediment and water discharge) have an influence on the downstream variables (basin accommodation, morphology and stratigraphy). This is a modification of the ubiquitous source-to-sink paradigm (Allen, 2008) on Earth wherein the ocean can be considered an infinitely large "sink" and fluvial discharge does not appreciably modify base level. In the crater-fill basin case water discharge and sediment flux "compete" for accommodation within the crater with the potential to cause more complex interactions and stratigraphy than a similar basin setup for a marine basin on Earth, which would simply result in progradational patterns.

3. Methods

3.1. Experimental Setup

The experiments were conducted in an acrylic flume (50 cm wide; 167 cm long; 45 cm depth) within the Western Washington University Experimental Earth Surface Laboratory (WEESL). Sediment and water were supplied to the flume through a Schenck AccuRate sediment feeder and a gauged head tank (Figure 1). The sediment was a 60:40 mixture of silica sand (D_{50} = 20 μm, ρ = 2.65 g/mL) and anthracite coal (D_{50} = 30-50 μm, ρ = 1.3 g/mL) representing a coarse-grained and fine-grained mixture, respectively. This is a similar approach to numerous previous experimental studies of fluvio-deltaic evolution (Muto and Steel, 2001b, 2004; Paola et al., 2009; de Villers et al., 2013). The sediment and water were separately fed into a plastic funnel that sat atop a cylindrical rock crib (35 cm tall; 10 cm diameter) situated at the proximal end of the flume. The rock crib was filled with gravel to disrupt the discharged dry sediment mixture and water from the overlying feeder funnel, allowing the experimental deltaic surface to spontaneously generate channels and overland flow. At the distal end of the flume a cylindrical weir (1.5 cm diameter) was inserted to act as the spill-point within the hypothetical crater basin (Figure 1). The weir's vertical height represents base level for the basin. For the experimental runs in Flume 1 (i.e., 1A, 1B, 1C) the weir height was set to 18.5 cm and for the experiments run in Flume 2 (i.e., 2A, 2B) the weir height was set to 22.7 cm, constituting a "small" and "large" crater, respectively. All other

dimensions of the flume were kept constant, meaning only the total accommodation between the two sets of experimental runs differed. All experiments had an initial sediment layer of dry, pure silica sand that was ~1.5 cm thick on the base of the flume prior to the start of each run. Amongst the five experiments the initial basin slope of the basal sediment layer (2º away from rock crib) and a constant water discharge (Q_w = 0.8 L/min) throughout the run. Sediment supply (Q_s) was increased by approximately 30% between each set of experiments. For experiments 1A and 2A Q_s was 0.13 L/min, for 1B and 2B Q_s was 0.19 L/min and for 1C Q_s was 0.22 L/m. Sediment feed rates remained constant throughout each individual experimental run (Table 1). Therefore, while an experiment was being run, all inputs (Q_s and Q_w) were constant, meaning any deltaic dynamics were caused by autogenic forcings and interactions of basin volumetrics.

All experiments were recorded in real-time from an overhead view using a SONY HDR - PJ670 digital video camera. Initial base level was marked before the start of each run and base level rise was recorded every 30 min for the duration of each run. After the weir was breached and significant progradation of the delta was observed, all inputs were stopped, and the experiment was left overnight to allow settling of all suspended sediment. The flume was then slowly drained of all water and left for two days to allow to partial drying without disturbing the deposited sediment.

3.2. Data Collection

Each flume was transported to the Mount Baker Imaging Center in Bellingham, Washington, where they were submitted to a Computed Tomography (CT) scan using the Siemens SOMATOM CT Scanner. Each experimental delta was visually inspected after transport to ensure no sediment was significantly disrupted before undergoing the scanning process. CT scanning is a noninvasive examination technique, mainly used in the medical industry on human subjects, that uses specialized X-rays to produce multiple cross-sectional images of a subject (Deng and Nadrlijanski, 2019). The images produced are based on a calculation of how easily a material can be penetrated by X-rays, known as the attenuation coefficient. The approach is commonly applied as a non-destructive means to examine fossilized material in the paleontological community and the internal structure of cores within the sedimentologic community (e.g., D'Emic et al. 2013; Gagnoud et al., 2009). The calculated penetration of X-rays can be equated to the density of the material (Deng and Nadrlijanski, 2019). The density contract between silica sand (ρ = 2.65 g/cm^3) and anthracite coal (ρ = 1.3 g/cm^3) is sufficient for a CT resolution of the internal deltaic

stratigraphy. Using a consistent scan parameter for a standard abdominal scan, all experimental data were produced as axial DICOM files with a slice thickness of 2 mm. Image clarity was diminished relative to typical paleontological and sedimentologic studies due to the retention of water that reduces the density contrast.

Each CT scan file was analyzed using Dragonfly™ image processing software from Object Research Systems. Dragonfly™ provides two-dimensional segmentation of the three-dimensional subject, creating interpretable cross-sectional images. For this study twenty two-dimensional cross section images were analyzed in a down-dip direction from the middle of each experiment (i.e., depositional dip parallel cross-sections). The twenty cross-sections were selected by finding the true middle slice of the data set and analyzing a cross-sectional image every 1.8 cm to the left and right until reaching the flume side barrier.

On each depositional dip cross-section delta shoreline positions were manually identified to produce twenty separate shoreline trajectories of the stratigraphy for each experimental run (Figures 2 and 3). The delta shoreline was manually identified as a break in slope from the delta topset to foreset deposits. For each experiment, all shoreline data points were extracted (Table 2), plotted by distance downstream and stratigraphic height, and quantitatively analyzed by their stratigraphic position. Compiling these separate measurements produces a "stack" of shoreline trajectories to produce a spatially "averaged" shoreline trajectory curve (Figures 3 and 4). The resulting curves were used to assess major depositional phases in delta evolution.

Additionally, cross-sections perpendicular to depositional dip (i.e., depositional strike cross-sections) were extracted and analyzed manually. The strike cross sections were extracted from the topset portion of each experiment, approximately 10 cm downdip of the rock crib. Major phases in deposition in each strike cross section were analyzed by sand-coal ratios, coal deposit geometries (i.e., aspect ratio of major-minor axes of bounding ellipse), stratigraphic surfaces, and the interpretation guided by the depositional phases identified in the depositional dip cross-sections (Figures 5 and 6). Major depositional phases were traced as surfaces and all coal deposits within each depositional phase were manually traced using Adobe Illustrator™ from strike cross-sectional images. The traced coal deposits were then extracted and analyzed using Image J™. Quantitative metrics obtained include the relative proportion of sand to coal during each phase, the number of distinct coal deposits in each phase, and the cross-sectional geometry of the coal deposits captured by the major – minor axis ratio of a bounding ellipsoid (Tables 3-7).

4. Results

4.1. Flume 1 "Small Crater"

Three separate experiments were run in Flume 1 (1A, 1B, 1C). Each experiment had 20 cross-sectional scans analyzed. Five major phases of deposition can be recognized based on the trajectory of the shoreline relative to the sediment source (i.e., rock crib): (1) early fluvial (2) mixed progradation (3) retreat (4) over-topping and (5) forced progradation (Figure 2). In addition, the approximate progradation, retrogradation, and aggradational thicknesses were tracked for each phase and relative proportion of silica sand and anthracite coal partitioned in each (Figure 6). Figure 4 shows shoreline trajectory data from each of the three experiments plotted with the x-axis as distance downstream (cm), 0.0 cm is proximal; the edge of the rock crib, and the y- axis as stratigraphic height (cm), 0.0 cm is the minimum; the top of the initial silica sediment layer. In total, 328 shoreline data points were extracted from Flume 1 experiments (Table 2).

4.1.1 Run 1A

4.1.1.1. Dip Cross Section Analysis

Phase one of Run 1A is comprised of flat-lying, silica-rich, proximal sheet-like deposits with coal accumulated on the distal end (Figure 2A). The first signs of scouring are seen in phase one along with thin, low angle (< 1 cm: < 1º) coal layers forming on the weak, distal foresets during phase one. Based on overhead video this phase was dominated by proximal channelization and distal sheet-flow, with early infiltration of water observed. Phase two begins with the first deltaic deposition of both topset and foreset with a distinct shoreline break. Silica sand occurs throughout the topset and foreset with coal accumulations appearing at the very distal end of the foreset. This two-part sediment partition pattern occurs in the following phases as well; three, four and five. Phase three is characterized by retrogradation overall, relatively thin foreset deposits, and thick topset deposits. Phase four displays a progradational pattern with thicker foresets and thinner, relatively sand-rich topsets. Finally phase five displays a progradation pattern with thick foresets and topsets characterized by scours and abundant quartz sand deposition.

4.1.1.2. Shoreline Trajectory

On average, Run 1A had five traceable shoreline points per dip section, yielding a total of 119 delta shoreline data points (Table 2). The stacked shoreline data shows five phases of deposition (Figure 4A). Phase one, early fluvial, was dominated by channel deposits that prograded

and aggraded the initial shoreline ~31.5 cm and ~11.8 cm, respectively. Phase two, mixed progradation, has a diffuse boundary that beings during phase one, as this phase consists of both channel and deltaic deposits. The mixed progradation phase caused the shoreline to prograde 11.1 cm and aggrade an additional 2.3 cm from its previous position. The shoreline trajectory then changed during phase three, retreat, that consisted of combined retrogradation and aggradation. The maximum retreat length of the shoreline was 8.0 cm with aggradation of 11.0 cm from its previous position. Following the shoreline retreat, phase four, over-topping was initiated with the shoreline shifting distally 9.4 cm and aggrading 3.3 cm from its previous position. Phase five, forced progradation, then transitioned into shoreline shift 7.9 cm basin-ward from its previous position.

4.1.1.3. Strike Cross-Section Analysis

Phase one of Run 1A is comprised of low angle, silica sand, sheet-like deposits separated by thin laterally continuous anthracite coal layers (Figure 6A). A sharp erosional contact marks the transition of phase one to phase two. Phase two shows similar depositional partitioning as phase one, except deposits in phase two were laterally dipping at a slightly steeper angle (i.e., development of a foreset). A diffuse, gradational contact separates phase two and three. Phase three presented a gradual change from deposits like phase two, with greater amounts of silica sand bodies with thin lenses of coal dispersed in the topset. A diffuse contact exists between phase three and phase four. Phase four is dominated by an amalgamation of silica sand bodies with no prominent depositional coal features. A sharp erosional contact separates phase four and phase five. Phase five has extensive in width (4 – 7 cm) lenticular silica sand bodies, with surrounding scoured zones of anthracite coal.

4.1.1.4. Quantitative Analysis of Coal Deposits

The total cross-sectional area of coal in the strike section in the proximal portions of the fluvio-deltaic stratigraphy is 25.0% for Run 1A (Table 3). Coal deposits make up 32.0% of the phase one cross-sectional area. There is a decrease to 26.0% in phase two, and a continued decrease in phase three to 22.0%. Phase four has the lowest coal cross-sectional area of 6.0%, and during phase five total coal area increases to 29.0%. The cross-sectional area of individual coal bodies shows a similar pattern. The average cross-sectional area of individual Phase one coal bodies (n=10) (normalized to the cross-sectional area of Phase 1) is 3.0% ± 2.0 (1σ, one standard deviation) (Table 4). In phase two (n = 20 coal bodies) the average cross-sectional area decreases

to 1.0% ± 1.0% (1σ) and stays at this average value for phase three (n = 15) and four (n = 10). During phase five (n = 13) the normalized cross-sectional area of coal bodies increases to 2.0% ± 4.0% (1σ). The geometry of the coal bodies also changes amongst the phases. In phase one the average aspect ratio of the best-fit ellipsoidal major-minor axes to the coal deposits is 7.9 ± 4.8 (1σ) (Table 6). In phase two this drops to 6.6 ± 2.8 (1σ) and in phase three 7.1 ± 3.5 (1σ). During the phase four aspect ratio drops to 3.8 ± 2.2 (1σ) in phase five it is 4.4 ± 2.3 (1σ).

4.1.2 Run 1B

4.1.2.1. Dip Cross Section Analysis

Phase one of Run 1B is silica sand-rich with laterally continuous low angle thin coal layers separating each sheet-like deposit (Figure 2B). The same partitioning of sediment continues into phase two, however the deposits are deltaic with a distinct topsets and foresets. A shift in the partitioning of sand and coal dominated topset and foreset occurs in phase three, there appears to be subequal partitioning of both topsets and foresets. The shoreline breaking point positions are coal dominated, and the foresets transition into amalgamations of silica and coal. In phase four the topset transitions to more silica rich and the foreset remains like the phase three foreset. During the latter half of phase four and all of phase five, the topsets and foresets are silica sand dominated, with thicker foreset that prograde.

4.1.2.2. Shoreline Trajectory

Seven traceable shoreline points per dip cross-section were found on average with Run 1B, making a total of 149 delta shoreline data points (Table 2). The compiled shoreline positions show five phases of deposition (Figure 4B). Phase one prograded and aggraded channel deposits ~47.5 cm and ~10.5 cm, respectively. Mixed progradation phase two extended the shoreline basin-ward an addition 2.7 cm and aggraded it 2.1 cm. The maximum retreat shifted the shoreline 13.7 cm inland and caused aggradation by 11.1 cm. Phase four continued to increase in aggradation by 2.8 cm with progradation of 2.3 cm. Lastly, the forced progradation phase extended the shoreline by 15.7 cm to its final trajectory position.

4.1.2.3. Strike Cross Section Analysis

Phase one of Run 1B is comprised of flat laying, silica sand, sheet-like deposits separated by thick laterally continuous anthracite coal layers (Figure 6B). A sharp erosional contact marks the transition to phase two where laterally dipping silica sand sheets are interbedded with thin coal lenses. A diffuse contact separated phase two and phase three. Phase three shows a gradational

change from an amalgamated silica sand with thin coal lenses, to lenticular silica sand bodies surrounded by thick laterally continuous coal deposits. A sharp erosional contact separates phase three and phase four. Phase four shows laterally extensive tabular silica sand deposits with thin coal lenses interspersed throughout. Lastly, a sharp erosional contact separates phase four and phase five. Phase five is consistent with phase four being made up of thick laterally continuous tabular silica sand bodies, however, phase four is lacking in coal deposits.

4.1.2.4. Quantitative Analysis of Coal Deposits

The total cross-sectional area of coal in the strike section in the proximal portions of the fluvio-deltaic stratigraphy is 21.0% for Run 1B (Table 3). Coal deposits make up 27.0% of the phase one cross-sectional area. There is a decrease to 18.0% in phase two, and an increase in phase three to 24.0%. Phase four shows a slight decrease to 21.0% and during phase five there is significant decrease to the lowest coal cross-sectional area of 11.0%. The cross-sectional area of individual coal bodies shows a consistency throughout the run. The average cross-sectional area in phase one (n= 13) is 2.0% ± 3.0 (1σ) (Table 4). The average cross-sectional area of phase two (n= 18) is 1.0% ± 1.0 (1σ). Phases three (n = 21) and four (n = 21) have average cross-sectional areas of 1.0% ± 2.0 (1σ). Phase five (n = 22) has the smallest average cross-sectional area of 0.5% ± 1.0 (1σ). The geometry of the coal bodies also remains show some consistency throughout the phases. Phase one has an average aspect ratio 5.5 ± 4.3 (1σ) (Table 6). Phase two slight decreases to an average aspect ratio of 5.3 ± 3.0 (1σ) and phase three increases to 5.6 ± 3.8 (1σ). Phase four and five show a large decrease in the average aspect ratio to 4.8 ± 3.1 (1σ) and 3.6 ± 2.7 (1σ), respectfully.

4.1.3 Run 1C

4.1.3.1. Dip Cross Section Analysis

Phase one of Run 1C has silica sand rich sheet deposits with thin, laterally continuous, low angle coal layers separating each deposit (Figure 2C). This partitioning pattern continues into phase two, as the deltaic deposits become slightly more distinct with the positioning of the topset and foreset. Phase three and phase four have a diffuse boundary with similar depositional patterns showing deep (1-2 cm) and laterally extensive scour traces, starting at the proximal side of the topset and continuing throughout. These scour traces are seen where thick coal layers exist in the predominantly silica sand topsets. The foresets during phase three and phase four are dominated

by aggregated anthracite coal deposits. Phase five shows similar topset partition patterns as phases three and four. Phase five foresets show alternating, laterally continuous, silica and coal deposits.

4.1.3.2. Shoreline Trajectory

Three traceable points per slice were extracted from Run 1C, totaling 60 delta shoreline data points (Table 2). The compiled shoreline positions show five phases of deposition (Figure 4C). Early fluvial prograded and aggraded channel deposits ~55.5 cm and ~10 cm, respectfully. Mixed progradation extended the shoreline downstream an addition 1.2 cm and aggraded it 1.1 cm. The most proximal autostepping retreated the shoreline 15.3 cm and increased aggradation by 5.9 cm. Over-topping caused progradation by 11.2 cm with aggradation of 7.5 cm. Lastly, force progradation extended the shoreline by 14.0 cm to its final trajectory position.

4.1.3.3. Strike Cross Section Analysis

Phase one of Run 1C is comprised of an amalgamation of flat laying silica sand and anthracite coal deposits (Figure 6C). A sharp erosional contact is separating phase one and phase two. Phase two consist of low angle, obliquely dipping, lenticular silica sand bodies with thick anthracite coal contacts around each sand lens, creating a stacking pattern throughout the phase. A sharp erosional contact is separates phases two and three. Phase three has similar partitioning to phase two, however the sand lenses are interconnected, creating amalgamated sand packages that are more laterally continuous. A sharp erosional contact is separating phase three and phase four. Phase four shows extensive signs of scouring. Due to this reworking, there are silica sand lenses with gradational anthracite coal pockets between them. A diffuse, highly eroded contact transitions phase four into phase five. Phase five has tabular silica sand bodies with thin coal layers acting as the contact between each sand body.

4.1.3.4. Quantitative Analysis of Coal Deposits

The total cross-sectional area of coal in the strike section in the proximal portions of the fluvio-deltaic stratigraphy is 29% for Run 1C (Table 3). Phase one coal deposits have a cross-sectional area of 31% which stays consistent through phase two at 31%. Phase three cross-sectional area slightly decreases to 27%. Then phase four increases to the highest cross-sectional area of 32%. Lastly, phase five decreases to 28%. The average cross-sectional area of individual phase one coal bodies (n=17) is 2.0% ± 2.0 (1σ) (Table 4). Phase two (n= 16) remains the average cross-sectional area at 2.0% ± 4.0 (1σ) and then decreases in phase three (n= 24) to 1.0% ± 2.0 (1σ). Phase four (n= 9) increases to the highest average cross-sectional area of 4.0% ± 4.0 (1σ) then

decreases in phase five (n= 21) to 1.0% ± 4.0 (1σ). In phase one the average aspect ratio of the coal bodies is 2.8 ± 1.7 (1σ) (Table 6). The average aspect ratio increases in phase two to 3.3 ± 2.8 (1σ). The increasing continues into phase three 4.0 ± 2.0 (1σ) and phase four 4.5 ± 2.2 (1σ). Lastly, phase five has a decrease in average aspect ratio to 3.6 ± 2.5 (1σ).

4.2. Flume 2 "Large Crater"

Two separate experiments were run in Flume 2 (2A and 2B). Each experiment had 20 cross-sectional scans analyzed. Five major phases of deposition can be recognized: (1) early fluvial (2) mixed progradation (3) retreat (4) over-topping and (5) force progradation (Figure 3). In addition, the approximate progradation, retrogradation, and aggradational thicknesses were tracked for each phase and relative proportion of silica sand and anthracite coal partitioned in each (Figure 7). Figure 5 shows shoreline trajectory data from each of the three experiments plotted. In total, 244 shoreline data points were extracted from Flume 2 (Table 2).

4.2.1 Run 2A

4.2.1.1. Dip Cross Section Analysis

Phase one of Run 2A has silica sand rich sheet deposits with thin, laterally continuous, low angle coal layers separating each deposit (Figure 3A). This partitioning pattern continues into phase two, as the deltaic deposits become slightly more distinct with the appearance of the topset and foreset. During phase three, three "micro-phase" transitions are seen in the stratigraphy. Micro-phases one and two have the same deposits; an initial small pulse of anthracite coal on the proximal side of the topset. Moving basin-ward the topsets become silica sand dominated and remains this way into the proximal portion of the foresets. The most distal end of the foresets are where accumulations of anthracite coal are located. Micro-phase three differs from the previous two with thick laterally continuous anthracite coal layers, with scouring, prominently seen separating silica sand deposits throughout the topsets. The foresets in micro-phase three are partitioned by the proximal portion being an amalgamation of silica sand and anthracite coal, and the distal portion is exclusively anthracite coal. Phases four and five have topsets and foresets that are silica sand dominated with the thin coal layers reappearing throughout.

4.2.1.2. Shoreline Trajectory

On average, Run 2A had six traceable points per slice, giving a total of 123 delta shoreline data points (Table 2). The compiled shoreline positions show five phases of deposition (Figure 5A). Phase one, early fluvial, was dominated by channel deposits that prograded and aggraded the

initial shoreline ~40.0 cm and ~10.0 cm, respectfully. Phase two, mixed progradation, has a diffuse boundary that beings during phase one, as this phase consists of both channel and deltaic deposits. The mixed progradation phase caused the shoreline to prograde 5.1 cm forward and aggraded the delta an additional 4.2 cm. The shoreline trajectory then changed during phase three, retreat, which consisted of three micro-phases. The first micro-phase retreated the shoreline 9.0 cm with aggradation of 4.0 cm. The second micro-phase caused the shoreline to prograde 6.0 cm with continued aggradation of 4.5 cm. The last micro-phase was retrogradational and moved the shoreline back another 6.5 cm with 3.7 cm of aggradation. Phase four, over-topping, caused progradation of 2.5 cm and aggradation of 3.8 cm. Over-topping then transitioned into progradation under steady state conditions, forced progradation, until the experiment was stopped. This final phase extended the shoreline basin-ward by 9.8 cm.

4.2.1.3. Strike Cross Section Analysis

Phase one of Run 2A has flat lying silica sand sheet deposits with thin, laterally continuous, coal layers separating each deposit (Figure 7A). A sharp erosional contact separates phase one and phase two. Phase two is comprised of thin, tabular, low angle, silica sand bodies with thin, extended coal lenses partitioned throughout. A diffuse erosional boundary exists between phase two and phase three. Phase three is composed of stacked obliquely dipping tabular sand bodies with thick, highly scoured coal layers between each sand body. A sharp erosional contact separates phase three and four. Phase four has amalgamated silica sand lenses with small coal pockets interspersed. Phase five has a very diffuse contact with phase four and shows similar depositional partitioning.

4.2.1.4. Quantitative Analysis of Coal Deposits

The total cross-sectional area of coal in the strike section in the proximal portions of the fluvio-deltaic stratigraphy is 26% for Run 2A (Table 3). The coal deposits during phase one make up 15.0% of the cross- sectional area. There is an increase to 27% of the cross-sectional area in phase two which stays the same in phase three. Phase four slightly increases to 28% and then phase five greatly increases to the highest cross-sectional area at 39%. The cross-sectional area of individual coal bodies shows a similar pattern. Phase one (n= 17) has an average cross-sectional area of 1.0% ± 1.0 (1σ) (Table 5). Phase two (n=17) increases slightly to 2.0% ± 2.0 (1σ) and then drops back to 1.0% ± 2.0 (1σ) during phase three (n= 26). Then there is a large increase in phase four (n=7) to an average cross-sectional area of 4.0% ± 6.0 (1σ) that continues to increase into

phase five (n=7) 6.0% ± 12.0 (1σ). However, the geometries of the coal bodies do not show an incrementally increasing pattern. The average aspect ratio for phase one 5.5 ± 3.1 (1σ) (Table 7). This increases in phase two to 6.1 ± 5.0 (1σ) and slightly decreases in phase three to 5.8 ± 3.6 (1σ). Phase four shows a large decrease to 3.9 ± 1.6 (1σ) and then a slight increase to 4.2 ± 2.6 (1σ) in phase five.

4.2.2 Run 2B

4.2.2.1. Dip Cross Section Analysis

Phase one of Run 2B has silica sand rich sheet deposits with thin, laterally continuous, low angle coal layers separating each deposit (Figure 3B). This partitioning pattern continues into phase two, as the deltaic deposits become slightly more distinct with the positioning of the topset and foreset. During phase three, three micro-phase transitions are seen in the stratigraphy. Micro-phase one shows silica sand dominated topsets until the distal portion, which is made of anthracite coal accumulations. This anthracite coal influence continues into the proximal portion of the foresets. However, on the distal end of the foresets the deposits change back to silica sand dominated. Micro-phase two and three have similar stratigraphy, where the topsets are mainly composed of silica sand, with very thin and short anthracite coal scattered throughout. The foresets of micro-phases two and three are the opposite of the topsets, showing anthracite coal dominated with small lenses of silica sand. Phases four and five have topsets and foresets that are silica sand dominated with the thin coal layers reappearing throughout.

4.2.2.2. Shoreline Trajectory

Six traceable points per slice were found on average for Run 2B, making a total of 121 delta shoreline data points (Table 2). The compiled shoreline positions show five phases of deposition (Figure 5B). Early fluvial prograded and aggraded channel deposits ~54.2 cm and ~11.5 cm, respectfully. Mixed progradation extended the shoreline downstream an additional 3.1 cm and aggraded it 1.5 cm. The shoreline trajectory then changed during phase three, retreat, which consisted of three micro-phases. The first micro-phase retreated the shoreline 13.8 cm with aggradation of 9.0 cm. The second micro-phase caused the shoreline to prograde 9.1 cm with continued aggradation of 1.0 cm. The last micro-phase was retrogradational and moved the shoreline back by 8.8 cm with 6.2 cm of aggradation. Phase four, over-topping, moved the shoreline basin-ward 3.2 cm and continued aggradation by 4.3cm. Lastly, force progradation extended the shoreline by 8.8 cm to its final trajectory position.

4.2.2.3. Strike Cross Section Analysis

Phase one of Run 2B has low angle silica sand sheet deposits with thin, laterally continuous, coal layers (Figure 7B). A sharp depositional contact exists between phase one and phase two. Phase two is composed of laterally dipping, tabular silica sand bodies with a few very thin extensive coal layers. A diffuse contact separates phase two and phase three. Phase three is similar to the phase two depositional pattern, however the coal layers transitioned into very thin coal lenses interbedded throughout phase three. A sharp erosional contact exists between phase three and phase four. Phase four is partitioned as flat lying amalgamation of silica sand with thin coal lenses. A diffuse contact is present between phase four and phase five. Phase five has a largely similar depositional pattern as phase four, but coal deposits appear smaller and less laterally extensive.

4.2.2.4. Quantitative Analysis of Coal Deposits

The total cross-sectional area of coal in the strike section in the proximal portions of the fluvio-deltaic stratigraphy is 18% in Run 2B (Table 3). Coal deposits during phase one make up 28.0 % of the cross-sectional area. This greatly decreases to 12.0% in phase two with a slight increase in phase three to 18.0%. There is a small decrease to 17.0% in phase four with a minimal increase in phase five to 19.0%. Phase one coal deposits (n = 11) have an average cross-sectional area of 3.0% ± 2.0 (1σ) (Table 5). Phase two (n= 12) has a decrease in average cross-sectional area to 1.0% ± 1.0 (1σ). This average cross- sectional area remains the same in phase three (n =28), phase four (n= 25) and phase five (n=21). The geometry of the coal bodies shows a similar pattern to the cross-sectional area through the phases. Phase one average aspect ratio is 4.9 ± 4.0 (1σ) (Table 7). Phase two has an increase to 7.0 ± 3.8 (1σ). Phase three remains at the same average aspect ratio of 6.9 ± 3.4 (1σ) then decreases in phase four to 4.4 ± 2.0 (1σ). Lastly, phase five is also consistent at an average aspect ratio of 4.2 ± 1.8 (1σ).

5. Discussion

5.1. Sequence Stratigraphy Analysis

Our results show that five stratigraphic sequence phases were consistently produced by experimental runs: (1) early fluvial (2) mixed progradation (3) retreat (4) over-topping and (5) forced progradation. The conceptual framework of each phase can be seen in Figure 8, where the sequence stratigraphy is schematically represented. Importantly, these patterns occur within a

"closed" basin wherein all sediment and water is trapped within a basin that passively receives sediment until the spill-point was reached. This is in contrast to Earth's marine sedimentary basins, which are typically “open” systems. Open systems are subject to external conditions such as eustatic influence that ultimately drives the depositional processes, but changes in fluvial discharge do not appreciably alter eustasy. From an "Earth-based" marine sedimentary basin perspective the stratigraphic patterns observed in the experiments easily fit within a classic sequence stratigraphic framework, which commonly invokes eustasy as the driving mechanism. This eustatic, allogenic forcing may include sea level variation by glacial ice sheet dynamics, ridge spreading, tectonic uplift and basin subsidence (Rovere et al., 2016). If the experimental fill was interpreted as if it were an Earth-based deltaic system, the following inferences would likely be made:

Phase one, early fluvial would begin when sea level is at its lowest with fluvial deposition is occurring. In a marine basin this might be linked with initial basin formation via extensional processes and rifting process. Commonly, within the early phases of marine rifting significant accumulations of evaporitic strata are deposited and playa deposits. Typically, catchments are small, and sediment supply low, but generation of accommodation space is fast due to lithospheric thinning. As eustatic sea level rises and transgression may take place, phase two, mixed progradation is initiated. Within an Earth marine basin this rapid increase in sea level could be interpreted as being caused by marine inundation that occurs post-oceanic rift or potentially the onset of an interglacial period or increased basin subsidence caused by lithosphere movement in a more mature sedimentary basin. Transgression continues with sea level rising through phase three, retreat, until a maximum flooding surface is reached and phase four develops. A classic sequence stratigraphic assessment of this pattern would invoke a sea-level rise followed by partial fall to produce the stratigraphic pattern. This could be due to long-term interglacial-to-early glacial period (i.e., high stand stage to falling stage) related to eccentricity-scale ice sheet dynamics on Earth (~100 kyrs) or potentially changes in mid-ocean ridge production. Lastly, phase five, forced progradation, would likely be interpreted as a "forced regression" and attributed to regrowth of an ice sheet (i.e., major glacial period) or significant reduction in midocean ridge spreading rates causing a regression with isostatic rebound. Of course, in our experiments none of these external factors or boundary conditions were modified or adjusted, but the stratigraphic pattern occurs regardless. This highlights the phenomena of "convergence" wherein several different factors can result in nearly identical stratigraphic sequences. Without a prior knowledge that this is a crater

fill with no eustatic control, a simple application of Earth-based interpretations would lead one to an incorrect allogenic reconstruction.

Now let us take the case of a sequence stratigraphic interpretation postulated by a martian stratigraphers. The likely approach would be that these phases were created by variations in lake level conditions. Martian lacustrine environments will form in crater-fill basins, which act as closed systems that experience base level rises and falls due to climatic conditions. The climatic interpretation of these sequences would begin with persistent warmer and wetter periods to provide sediment and water volumes that can achieve sufficient base level rise, as well as high erosion rates to deposit phases one through three. As seen in the experiments of DeVilliers et al. (2013) and Kraal et al. (2008), reduction in sediment supply as erosive canyon river systems reach closer to equilibrium profiles exacerbate this base level rise. Following this would be periods of cold and dry conditions that force increased evaporation rates to occur, accounting for base level fall. While excess evaporation takes place, erosion rates must also remain high to produce enough sediment supply to the crater to deposit phases four and five, and cause progradation. A "forced regression" occurs when evaporation exceeds precipitation.

The experiments presented herein argue a martian crater-fill basin is a closed system that can experience variations in base level due and spontaneous development of stratigraphic sequences as a consequence of sediment and water discharge interacting with the accommodation space (Figure 8). The interpretation for this mass balance transfer begins with a set crater basin accommodation volume. During phase one, the water volume infiltrates as groundwater while sediment simultaneously extends along the basin floor, prograding without the hinderance of a base level volume. Once the basin floor quickly reaches saturation, water input volume is strictly contributing to continuous base level rise. As base level reaches an appropriate height, the sediment inputs begin partitioning into topset and foreset domains, which through time create phase two, mixed progradation. Progradation incrementally forces sedimentation basin-ward, creating thinner topsets and thicker foresets through time. The system will continue to deposit more sediment on the foreset, until finally “starving” the topset of all sediment which allows for the water volume to takes its place and flooding to occur. This first flooding surface marks the transition into phase three, retreat, when the rising base level is shifting the shoreline land-ward which evidently constrains sedimentation to a smaller accommodation volume. As the sediment retreats with the shoreline it is repeatedly deposited above the previous topset and may form a

back-stepping or auto-stepping morphology (Muto and Steel, 2001b). Phase three continues until the total basin accommodation volume is filled, leading to crater overspill, at which point base level has reached its maximum. The system will now continue under constant base level conditions, allowing for sediment volume to partially displace water volume. Sediment volume begins to extend the topset and foreset deposits onto the previously deposited delta submarine morphology, in turn triggering minor progradation that we see in phase four. While the system remains in equilibrium, phase five, forced progradation, steadily pushes the shoreline basin-ward due to sediment volume replacing water volume by burying primary fan morphology with newly formed thin topset and thick foreset deposits. Overall, martian crater-fill basins have the potential to produce complex stratigraphic sequences under constant boundary conditions. Therefore, we propose that future martian deltaic analysis be primarily viewed as a possible simple closed system, opposed to a starting asssumption of allogenic drivers.

5.2. Lithologic Pattern Predictions

Experimental delta fan morphology and associated stratigraphy was formed due to the system's ability to partition sediment types. Sediment types included a silica sand and anthracite coal representing a bi-modal density distribution of coarse-grained and fine-grained material, which can be used to hypothesize on the stratigraphic patterns produced by more complex field-scale systems. Two hypothetical stratigraphic sections are presented to show the correlated proximal and distal facies (Figure 9) with associated lithofacies and structures found in Table 8. Phase one is represented by a channel fills forming fluvial facies at the proximal location and mudstone and evaporite couplets producing playa facies at the distal location. As base level rises, a flooding surface is created and thin laminated mudstones with interbedded turbidites are predicted to deposited proximally by prodelta facies while thin interbedded very fine sandstones and mudstones are deposited distally by shallow lacustrine facies. Both lithofacies begin with thin bedding and increase to thicker beds as base level rises. When base level reaches an appropriate depth where progradation becomes sustainable, the proximal facies transitions to steeply dipping (~30º) fine grained sandstone beds from the delta front facies, while the distal location transitions to the prodelta facies. Bed thickness for both lithofacies incrementally increase as base level rises. As phase two mixed progradation advances, the delta front facies continue at the proximal location until transitioning to coarser grained sandstone, slightly less inclined, deposited by the delta plain facies. Throughout the proximal facies change, the distal location is a delta front facies that

increases its bed thickness throughout the phase. At the end of phase two, progradation has reached its maximum extent, and a flooding surface is formed as retrogradation begins marking phase three. As the shoreline retreats through phase three, lithofacies decrease from delta front to prodelta, with possible flooding surfaces representing facies change. Beds within associated lithofacies begin thick and incrementally become thinner, until aggradation is reached at the end of the phase three prodelta facies. At the distal location, interbedded turbidites and mudstones are deposited throughout phase three from deep lacustrine facies. Lastly, during phases four and five, progradation returns, developing an increasing pattern of delta front to delta plain and ending with fluvial facies. An increasing progradational pattern also forms at the distal location with prodelta to delta front and ending with delta plain facies.

5.3. Literature Interpretations of Martian Crater Basin Stratigraphy

5.3.1. Eberswalde Crater

Eberswalde crater is a quasi-circular impact crater, to the northeast of Holden crater, located within the Erythraeum region of Mars (Grant and Parker, 2002). Eberswalde crater is estimated to have formed in the Late- Noachian to Early Hesperian (~3.5 Ga) and has major and minor axes lengths of approximately 70 km and 50 km, respectively, with a maximum depth of ~1.2 km (Moore et al., 2003; Rice et al., 2012). The crater is topographically divided into two main basins: the "Western Basin" and the "Eastern Basin" (Figure 10; Rice et al., 2011). Data produced from orbiters and martian rovers such as High Resolution Imaging Science Experiment (HiRISE), Context Camera (CTX) images, and HiRISE digital terrain models (DTMs) has allowed researchers to identify and analyze six major fluvio-deltaic systems within the Western Basin (Malin and Edgett 2003; Moore et al. 2003; Bhattacharya et al. 2005; Wood 2006; Lewis and Aharonson 2006; Pondrelli et al. 2008; Pondrelli et al. 2011; Rice et al., 2011; 2013; Goddard et al., 2013). We will focus on discussing two of the six systems within the basin: the southwestern system and the western system. Goddard et al. (2013) present a detailed interpretation of the southwest system using facies analysis that is built upon the Rice et al. (2011; 2013) facies framework. While many researchers have analyzed the western deposit, we will focus on the Pondrelli et al. (2008) interpretation as it presents sequence stratigraphic analysis for deltaic formation.

Goddard et al. (2013) identified multiple facies and their associated contact relationships across three main transects of the southwest system. Within said transects, the most applicable

facies discussed for our study is the Fractured, layered (FL) facies (Rice et al., 2013). Multiple FL facies were identified along all the three transects and analyzed as containing "stratal units" (SU), meaning visible layering of the rock type is observed. Overall, ten SU's were identified within the southwest system (Figure 11). Observing the system from the distal to the proximal locations, SU1 exists distally at the lowest elevation while proceeding SU's incrementally increase in elevation and shift towards the proximal direction, towards the crater rim (Figure 12). Goddard et al. (2013) describe and interpret each SU as the following:

SU1 is an elongated, flat-lying, ribbon-shaped sedimentary body that also overlies other flat-lying, possible basement rock. SU1 shows layer thicknesses of < 7 m and with available dip measurements. Goddard et al. (2013) interpret this deposit as a preserved fluvial channel. Moving proximally through the basin, SU2 is encountered next. SU2 is described as a lobate sedimentary body with a collection of elongated ribbon bodies that seem to extend from a singular location on the surface of the lobe. The deposits associated layers show thickness ranges from < 7m to < 12 m with an average dip of ~1.2º. Goddard et al. (2013) have interpreted this unit as a preserved deltaic lobe with surficial distributary channels bifurcating from a single node position. SU3 has a similar morphology to SU1 although it is shorter in length and slightly thicker (< 8 m). SU3 is therefore also interpreted as a fluvial channel. SU3 exists between SU2 and SU4 and is thought to be a connecting fluvial channel of the two deposits. SU4 and SU5 show similar morphologies to SU2. Differences occur as SU4 has an average dip of ~1.3º and layer thickness ranges from 8 m to 20 m, while SU5 has an average dip of ~1.7 º and layer thicknesses from 12 m to 16 m. SU4 and SU5 are also interpreted as deltaic lobes with multiple bifurcating distributary channels forming from a major node location. Goddard et al. (2013) recognize that the deposits of SU's 1 through 5 are positioned by their relative chronology based upon their cross-cutting relationship and relative elevations. SU1 is likely the oldest preserved deposit as it is the most distal and exists at the lowest elevation, with decreasing relative age from SU's 2 through 5. Goddard et al. (2013) then identify SU's 6 through 9 as also analogous of deltaic lobes with SU's 8 and 10 also partially presenting morphologies for fluvial channels. However, SU's 6 through 9 greatly contrast with the "type" of deltaic lobes that is presented from SU's 2, 4 and 5. For example, there is a lack of bifurcating distributary channels, overall increase in layer thicknesses (8 m to 35 m) and overall lobe geometry varies laterally. With these interpretations Goddard et al. (2013) predict that three depositional processes created such stratigraphic variations.

The first process indicates subaerial channel formation from an early stage intracrater lake beginning to form. As the lake continues to form, partially filling the Western Eberswalde basin the second process creating deltaic deposition occurs. The relative locations of at least five separate bifurcating nodes associated with the deltaic lobes of SU's 2 through 5 show increasing stratigraphic elevation and simultaneous proximal shifting through time. This is suggestive of a transgression deltaic system formed from continuous base level rise. Transgression may create autostepping, the process of deltaic lobe retreat creating a backward stepped morphology (Muto and Steel, 2001b), which Goddard et al. (2013) propose is represented from SU's 2 through 5. However, SU's 6 through 9 do not show signatures of lobe transgression based on the varying morphologies. Goddard et al. (2013) therefore hypothesize that the system experienced a period of regression, creating the later deposits of SU's 6 through 10.

The western system, or better known as the Eberswalde Delta, has been analyzed and interpreted to greater detail than that of the southwest system. Previous studies have mapped three (Bhattacharya et al., 2005) to five (Wood, 2006; Pondrelli et al., 2008; 2011) distinct delta lobes. Pondrelli et al. (2008) mapped four main deltaic lobes of the Eberswalde delta and applied associated sequence stratigraphic interpretations (Figure 13). Beginning with the presumed oldest deposit, Lobe A, this delta lobe is divided into the lower and upper sections. Pondrelli et al. (2008) have interpreted the lower section of Lobe A as a deltaic lobe that initially began depositing during transgression, as base level in the basin was beginning to rise. The boundary between the sections marks a potential maximum flooding surface in which case the systems base level continued to rise while a proposed increase in sediment supply was introduced (Pondrelli et al., 2008). This putative excess sediment supply allowed for progradation to occur and the upper section of Lobe A to be deposited. Located on the surface of Lobe A was interpreted meandering distributary channels. Lobe B was inferred to cross-cut Lobe A's meandering channels, indicating Lobe B is younger in age. Lobe B is interpreted to have been deposited with greater accommodation conditions compared to Lobe A, as it extends further out into the basin. The surficial distributary channels on Lobe B are thought to be braided channels which would correspond to higher discharge rates and channel gradients. With these combined inferences, Pondrelli et al. (2008) interpreted Lobe B as being deposited during a base level decrease in the system, which created forced regression. Lobe C overlies Lobe B, and is inferred to have meandering distributary channels as well as lower channel gradients, indicating a decrease in discharge compared to Lobe

B. The layers in Lobe C showed retrogradational stacking patterns which Pondrelli et al. (2008) interpreted as a base level increase and possible sediment supply decrease, creating transgression, in which Lobe C is deposited. Lastly, Lobe D is analyzed as degrading into previous deposits of Lobe B and C, as well as extending the furthest distally into the basin. Pondrelli et al. (2008) used these interpretations to support that Lobe D was deposited during a base level decrease which initiated forced regression. The sequence stratigraphic pattern presented by Pondrelli et al. (2008) suggests base level rises and falls by the allogenic forcings of either climatic or tectonic fluctuations.

5.3.2. Jezero Crater

Jezero crater exists in the Nili Fossae region of Mars and is estimated to have formed during the Late Noachian to Early Hesperian boundary (~3.8 Ga) (Fasset and Head, 2005). The crater is ~45 km in diameter and contains a large fluvial-deltaic deposit to the west (Figure 14), known as the Jezero Western Delta (JWD) (Fasset and Head, 2005; Schon et al., 2012; Goudge et al., 2017; 2018). JWD is interpreted to have been hydrologically fed by northern and western inlet valleys along the crater rim, and there is also evidence for a drainage valley to the east (Fasset and Head, 2005). Goudge et al. (2018) used detailed surface mapping and analysis to interpret the sequence stratigraphic framework that potentially formed JWD. Goudge et al. (2018) recognized the difference in preserved fluvial channel deposits from along the delta deposit surface. At lower stratigraphic elevations and seen distally in the basin the fluvial deposits were characteristic of a meandering channel system. In some locations below these meandering channel deposits, progradational deltaic lobes were also identified (Goudge et al., 2017). Moving proximally and at higher stratigraphic elevations, the fluvial deposits transitioned to a bifurcating and avulsing distributary channel system. Goudge et al. (2018) interpreted this morphologic change as being caused by the onset and continuation of base level rise within the basin. The continuous base level increase would create a transgressive environment, shifting the shoreline and its associated deposits proximally. Goudge et al. (2018) suggested this process occurred and the preserved deposits of JWD express morphologies of autostepping (Muto and Steel, 2001b). The increased avulsive nature of the distributary channels also indicate possible aggradation occurring during this transgressive succession. Fassett and Head (2005) previously identified an incised outlet valley to the east, being created by over-spill of the basin. Goudge et al. (2018) supported this interpretation as suggesting transgression continued until base level reached its maximum height

(i.e., Jezero basin rim) when a valley outlet on the eastern crater rim was formed. Goudge et al. (2018) suggested the inlet valleys did not experience input variations due to the outlet valley continued flooding, therefore creating a relatively fixed base level. Under such steady state conditions, regression occurred and prograded deltaic deposits distally into the basin. Goudge et al. (2018) hypothesized this last stage of the system based upon highly eroded lobate remnants found distally past the preserved JWD deposits. A secondary hypothesis of these distal deposits would be that there was a significant base level decrease produced from the valley outlet floods, however there are no large-scale unconformities observed on the JWD to support this inference. Therefore, Goudge et al (2018) concluded that progradation under steady state conditions occurred, and later a decrease in lake level or decrease in sediment supply occurred creating the youngest deposit of an incised valley on the surface while exposing JWD to aeolian activity to erode it to its present stratigraphic preservation.

5.4. Inferred Martian Depositional Conditions

The preservation and analysis of fluvial and deltaic stratigraphy on Mars has been the key proxy for understanding the planet's past climatic conditions. Many researchers have linked regional stratigraphic occurrence on Mars to major climate durations of a “wetter” and “drier” period. Mars’ wetter period is typically thought to span from the Early Noachian to the Early Hesperian (3.9 – 3.6 Ga) (e.g., Masursky 1973; Craddock and Maxwell 1993; Craddock and Howard, 2002; Forsberg-Taylor et al. 2004) and the drier period from the Late Hesperian to the modern day (3.4 – 0 Ga) (Zabrusky et al. 2012; Kite et al. 2017; Kite et al. 2019). Conflicting interpretations arise, however, when discussing regional climatic fluctuations within the wetter Mars period, based on analysis of sequence stratigraphy. For example, the sequence stratigraphic interpretations for the Southwest Eberswalde Deposit (SWE), Eberswalde Delta (ED) and the Jezero Western Delta (JWD) (Pondrelli et al., 2008; Goddard et al., 2013; Goudge et al., 2018) all present large-scale stratigraphic similarities, however the hypothesized duration and degree of climatic control varies when focusing on the intricate stratigraphic observations.

Beginning with the large-scale stratigraphic similarities, all three fluvio-deltaic systems have been interpreted as having early periods of transgression. During this transgressive period, all three systems show morphologies that are representative, to varying degrees, of autostepping (Muto and Steel, 2001b). Transgression is proposed to be the cause of consistent base level rise in each of the respective basins. This base level rise would suggest an initial period of wetter climate

(Pondrelli et al., 2008; Goddard et al., 2013; Goudge et al., 2018). The discrepancy arises when taking a closer look at the stratigraphic observations. The SWE and JWD's transgressive succession is seen as a single continuous wetting event and both systems presented similar transitions of delta lobe distributary channels changing from sinuous meanders to increased bifurcations and avulsions. Both systems also present older deposits underlying the transgressive strata that are interpreted as being mainly fluvial channels that formed during the onset of base level rise. However, ED's transgressive stratigraphy is divided into two wetting periods with a period of regressive deposition marking the stratigraphic separation. ED also has minimal observable evidence for preserved underlying fluvial channels. Therefore Pondrelli et al. (2008) suggested that there is a change in the climate, shifting to drier conditions, allowing for significant base level decrease and regression to occur. Following this short-term dry period, climatic conditions return to the wetter state, which instates base level rise, and transgression continues. This climate timeline presented by Pondrelli et al. (2008) varies from the climatic conditions interpreted by Goddard et al. (2013) for the SWE. Goddard et al. (2013) hypothesized a consistent wet period producing continuous base level rise and transgression, followed by a later regressive period that presents little evidence of a significant base level fall due to a drier climatic period. This is important to consider as these two deposits were both formed within the Eberswalde Western Basin. For this reason, we present the hypothesis that these sedimentary deposits may not have been produced by the allogenic force of a changing climate. Instead, the Eberswalde Western Basin stratigraphy was generated autogenically by the response of mass balance transfers during a continuous wetting period.

5.5. Experimental and Martian Stratigraphic Comparisons

The experimental outcomes of our study produced a period of transgression which we refer to as phase three, retreat. During phase three the shoreline and deltaic deposits were shifted proximally, creating an auto-stepped morphology in the system (Figure 8). However, the duration and degree of autostepping varied between the Flume 1 and Flume 2 experiments. The Flume 1 experiments presented a single continuous period of retreat, with low to medium sediment discharge rates (Q_s= 0.13, 0.19 L/min) producing clear autostepping patterns (Table 1). At the higher sedimentation rate (Q_s = 0.22 L/min), delta foreset morphologies were less traceable and autostepping was not clearly observed. Experiments in Flume 2 displayed clear autostepping patterns but on a smaller scale as three micro-phases occurred during the overall retreat period.

The microphases presented a pattern of retrogradational, progradational and finally retrogradational deposits, with an overall proximal shift of the shoreline (Figure 5). It is important to note that the stratigraphic pattern described by Pondrelli et al. (2008) required continual creation of accommodation and base level rise. The proposed regressions still occur during an overall sea level rise that allows the preservation of stratigraphy. The proposed unconformities within the strata identified by Pondrelli et al. (2008) necessitate sediment bypass to more distal portions of the crater, which should be recognizable within bed thickness patterns.

Prior to phase three, all experiments had an initial period of fluvial progradation referred to as phase one, early fluvial (Figure 8). Due to the non-cohesive properties of the sediment, distinction of fluvial channel type (i.e. meandering or braided) was not feasible. Following phase three, all systems produced a period of extensive progradation, when new deltaic clinoforms were deposited on top of previously created stratigraphy. This phase is referred to as phase five, forced progradation, as it occurred after base level reached a maximum and the system transitioned into steady state conditions (Figure 8).

Phases one, three and five in Flume 1 showed compelling sequence stratigraphic similarities to the interpreted stratigraphies of the Southwest Eberswalde Deposit and the Jezero Western Delta (Goddard et al., 2013; Goudge et al., 2018). While phases three and five in Flume 2 present sequence stratigraphic similarities to the interpreted stratigraphy of the Eberswalde Delta (Pondrelli et al., 2008). We predict that phase one, early fluvial is also associated with the Eberswalde Delta, however, it is not readily exposed in previously interpreted outcrop. Discrepancies of the experimental stratigraphy to the martian stratigraphy exist with phase two, mixed progradation and phase four, over-topping. Both phases existed as “transitional” phases in the experimental outcomes (Figure 8). Meaning, phase two was defined as the transition from fluvial deposition, phase one, to deltaic deposition, phase three. Phase four was then defined as the transition from phase three, retrogradational deposition with increasing base level, to phase five, progradational deposition, under steady state base level. Phase two and phase four were observed with very diffuse phase boundaries and lasting for short durations of time. Therefore, the lack of recognition between these phases and the interpreted martian stratigraphy may be due to multiple explanations. Firstly, these phase boundaries may not have been stratigraphically recognizable, as they have diffuse boundaries opposed to unconformities. Secondly, they may be preserved in the strata but have not been observed due to lack of exposure. Lastly, as these phases were of short

depositional durations, therefore they may exist in the martian stratigraphy below the present data resolution capabilities for interpretation.

Indeed, researchers have postulated that Mars intermittently existed with periods of warmer, wetter climatic conditions, potentially during the Early Noachian to the Early Hesperian (3.9 – 3.6 Ga) (Masursky 1973; Craddock and Maxwell 1993; Craddock and Howard, 2002; Forsberg-Taylor et al. 2004). If such wetting events occurred in pulses, interrupted by drier periods, crater-fill basins base levels would have the potential to significantly decrease. Based on DeVillers et al. (2013) experimental analysis, such base level decreases create extensive erosion of previously deposited stratigraphy, which would alter delta fan morphology. Extensive stratigraphic erosion of underlying deposits was not interpreted by Pondrelli et al. (2008), Goddard et al. (2013) or Goudge et al. (2018) when analyzing these martian crater-fill basins. Therefore, predictions that Mars' wetter periods were separated by lengthy periods of water loss (i.e. drought or high evaporation rates), is an insufficient analysis these warmer wetter martian events. On the contrary, Goudge et al. (2016) argued on the basis of an early Mars (~3.7 Ga), having fluvial activity that generated greater water influx rates within crater-fill basins due to extensive inlet valley networks. Such valley networks would produce crater-fill basins that could lead to over-topping and produce an outlet valley allowing for steady state base level during wetting events. Goudge et al. (2016) predicts over 200 martian crater-fill basins may have experienced such base level conditions from their associated wetting events. Thus, we suggest our autogenically produced sequence stratigraphic pattern constitutes as a "null" hypothesis for said crater-fill basins that are interpreted to have experienced a single, relatively persistent, Mars wetting event. We would predict the stratigraphy in the 200 crater-fill basins identified by Goudge et al. (2016) would display strong similarities to our experimental patterns.

6. Conclusion

Much of the observed crater -fill basin martian stratigraphy has been interpreted as a product of external large – scale allogenic forcing, specifically fluctuating climatic conditions. Through experimental analysis, we produced sequence stratigraphy under autogenic conditions that is comparable to this interpreted martian stratigraphy. Overall, the interpreted Mars stratigraphic patterns match our experimental depositional phases one, three and five, both in terms of the depositional environments, sequence boundary transitions and the general increase in each phases' stratigraphic thickness. Our experimental results also suggest that the overall sequence

pattern observed in these deltaic systems could simply be attributed to a steady base level rise and subsequent breaching of the basin, creating steady state conditions. Therefore, if the martian sequence stratigraphy presented is not a product of Mars climatic conditions than the alternative hypothesis is that it is a result of autogenic factors generated by continuous discharge conditions. In conclusion, it is suggested that future martian stratigraphic analysis consider extensive uninterrupted fluvial activity occurring during a warmer, wetter period in Mars' past.

References

Allen, P.A. (2008) From landscapes into geological history. *Nature 451*, 274-276.

Andrews-Hanna, J., & Lewis, K. (2011). Early Mars hydrology: 2. Hydrological evolution in the Noachian and Hesperian epochs. *Journal Of Geophysical Research*, *116*(E2). doi: 10.1029/2010je003709

Armitage, J., Duller, R., Whittaker, A., & Allen, P. (2011). Transformation of tectonic and climatic signals from source to sedimentary archive. *Nature Geoscience*, *4*(4), 231-235. doi: 10.1038/ngeo1087

Baker, V., & Partridge, J. (1986). Small Martian valleys: Pristine and degraded morphology. *Journal Of Geophysical Research: Solid Earth*, *91*(B3), 3561-3572. doi: 10.1029/jb091ib03p03561

Baker, V., Strom, R., Gulick, V., Kargel, J., Komatsu, G., & Kale, V. (1991). Ancient oceans, ice sheets and the hydrological cycle on Mars. *Nature*, *352*(6336), 589-594. doi: 10.1038/352589a0

Bhattacharya, J., Payenberg, T., Lang, S., & Bourke, M. (2005). Dynamic river channels suggest a long-lived Noachian crater lake on Mars. *Geophysical Research Letters*, *32*(10). doi: 10.1029/2005gl022747

Breuer, D., & Spohn, T. (2003). Early plate tectonics versus single-plate tectonics on Mars: Evidence from magnetic field history and crust evolution. *Journal Of Geophysical Research*, *108*(E7). doi: 10.1029/2002je001999

Cabrol, N., & Grin, E. (1999). Distribution, Classification, and Ages of Martian Impact Crater Lakes. *Icarus*, *142*(1), 160-172. doi: 10.1006/icar.1999.6191

Carr, M., Crumpler, L., Cutts, J., Greeley, R., Guest, J., & Masursky, H. (1977). Martian impact craters and emplacement of ejecta by surface flow. *Journal Of Geophysical Research*, *82*(28), 4055-4065. doi: 10.1029/js082i028p04055

Coe, A., Bosence, D., Church, K., Flint, S., Howell, J., & Wilson, R. (2005). *The sedimentary record of sea-level change*. Milton Keynes, U.K.: Open University.

Craddock, R., & Maxwell, T. (1993). Geomorphic evolution of the Martian highlands through ancient fluvial processes. *Journal Of Geophysical Research: Planets*, *98*(E2), 3453-3468. doi: 10.1029/92je02508

Craddock, R., & Howard, A. (2002). The case for rainfall on a warm, wet early Mars. *Journal Of Geophysical Research: Planets*, *107*(E11), 5-13 doi: 10.1029/2001je001505

D'Emic, M., Whitlock, J., Smith, K., Fisher, D., & Wilson, J. (2013). Evolution of High Tooth Replacement Rates in Sauropod Dinosaurs. *Plos ONE*, *8*(7), e69235. doi: 10.1371/journal.pone.0069235

De Villiers, G., Kleinhans, M. and Postma, G. (2013). Experimental delta formation in crater lakes and implications for interpretation of Martian deltas. *Journal of Geophysical Research: Planets*, 118(4), 651-670.

Duller, R., Whittaker, A., Fedele, J., Whitchurch, A., Springett, J., & Smithells, R. et al. (2010). From grain size to tectonics. *Journal Of Geophysical Research*, *115*(F3). doi: 10.1029/2009jf001495

Fassett, C., & Head, J. (2005). Fluvial sedimentary deposits on Mars: Ancient deltas in a crater lake in the Nili Fossae region. *Geophysical Research Letters*, *32*(14), 1-9doi: 10.1029/2005gl023456

Forget, F. (2009). The present and past climates of planet Mars. *The European Physical Journal Conferences*, *1*, 235-248. doi: 10.1140/epjconf/e2009-0924-9

Forsberg-Taylor, N., Howard, A., & Craddock, R. (2004). Crater degradation in the Martian highlands: Morphometric analysis of the Sinus Sabaeus region and simulation modeling suggest fluvial processes. *Journal Of Geophysical Research*, *109*(E5). doi: 10.1029/2004je002242

Gagnoud, M., Lajeunesse, P., Desrosiers, G., Long, B., Dufour, S., Labrie, J., Mermillod-Blondin, F., and Stora, G. (2009) Litho- and biofacies analysis of postglacial marine mud using CT-Scanning. *Engineering Geology 103,* 106-111.

Gobo, K., Ghinassi, M., & Nemec, W. (2014). Reciprocal Changes In Foreset To Bottomset Facies In A Gilbert-Type Delta: Response To Short-Term Changes In Base Level. *Journal Of Sedimentary Research*, *84*(11), 1079-1095. doi: 10.2110/jsr.2014.83

Gobo, K., Ghinassi, M., & Nemec, W. (2015). Gilbert-type deltas recording short-term base-level changes: Delta-brink morphodynamics and related foreset facies. *Sedimentology*, *62*(7), 1923-1949. doi: 10.1111/sed.12212

Goddard, K. (2013). The evolution of sedimentary systems on Mars, and implications for climate in the Hesperian-Amazonian epochs. (Doctoral dissertation). *Imperial College London,* 197-270

Goudge, T.A., Fassett, C.I., Head, J.W., Mustard, J.F., & Aureli, K.L. (2016) Insights into surface runoff on early Mars from paleolake basin morphology and stratigraphy, *Geology 44,* 419-422. doi:10.1130/G37734.1

Goudge, T., Milliken, R., Head, J., Mustard, J., & Fassett, C. (2017). Sedimentological evidence for a deltaic origin of the western fan deposit in Jezero crater, Mars and implications for future exploration. *Earth And Planetary Science Letters*, *458*, 357-365. doi: 10.1016/j.epsl.2016.10.056

Goudge, T., Mohrig, D., Cardenas, B., Hughes, C., & Fassett, C. (2018). Stratigraphy and paleohydrology of delta channel deposits, Jezero crater, Mars. *Icarus*, *301*, 58-75. doi: 10.1016/j.icarus.2017.09.034

Grant, J., & Parker, T. (2002). Drainage evolution in the Margaritifer Sinus region, Mars. *Journal Of Geophysical Research*, *107*(E9). doi: 10.1029/2001je001678

Grotzinger, J., Beaty, D., Dromart, G., Gupta, S., Harris, M., & Hurowitz, J. et al. (2011). Mars Sedimentary Geology: Key Concepts and Outstanding Questions. *Astrobiology*, *11*(1), 77-87. doi: 10.1089/ast.2010.0571

Haberle, R., McKay, C., Schaeffer, J., Cabrol, N., Grin, E., Zent, A., & Quinn, R. (2001). On the possibility of liquid water on present-day Mars. *Journal Of Geophysical Research: Planets*, *106*(E10), 23317-23326. doi: 10.1029/2000je001360.

Hajek, E., & Straub, K. (2017). Autogenic Sedimentation in Clastic Stratigraphy. *Annual Review Of Earth And Planetary Sciences*, *45*(1), 681-709. doi: 10.1146/annurev-earth-063016-015935

Hampson, G., Duller, R., Petter, A., Robinson, R., & Allen, P. (2014). Mass-Balance Constraints On Stratigraphic Interpretation of Linked Alluvial-Coastal-Shelfal Deposits From Source To Sink: Example From Cretaceous Western Interior Basin, Utah and Colorado, U.S.A. *Journal Of Sedimentary Research*, *84*(11), 935-960. doi: 10.2110/jsr.2014.78

Heller, P., & Paola, C. (1992). The large-scale dynamics of grain-size variation in alluvial basins, 2: Application to syntectonic conglomerate. *Basin Research*, *4*(2), 91-102. doi: 10.1111/j.1365-2117.1992.tb00146.x

Ingersoll, A. (1970). Mars: Occurrence of Liquid Water. *Science*, *168*(3934), 972-973. doi: 10.1126/science.168.3934.972

Irwin, R., Lewis, K., Howard, A., & Grant, J. (2015). Paleohydrology of Eberswalde crater, Mars. *Geomorphology*, *240*, 83-101. doi: 10.1016/j.geomorph.2014.10.012

Jerolmack, D., Mohrig, D., Zuber, M., & Byrne, S. (2004). A minimum time for the formation of Holden Northeast fan, Mars. *Geophysical Research Letters*, *31*(21), doi: 10.1029/2004gl021326

Jerolmack, D. (2009). Conceptual framework for assessing the response of delta channel networks to Holocene sea level rise. *Quaternary Science Reviews*, *28*(17-18), 1786-1800. doi: 10.1016/j.quascirev.2009.02.015

Karamitopoulos, P., Weltje, G., & Dalman, R. (2014). Allogenic controls on autogenic variability in fluvio-deltaic systems: inferences from analysis of synthetic stratigraphy. *Basin Research*, *26*(6), 767-779. doi: 10.1111/bre.12065

Kim, W., Paola, C., Swenson, J., & Voller, V. (2006a). Shoreline response to autogenic processes of sediment storage and release in the fluvial system. *Journal Of Geophysical Research*, *111*(F4). doi: 10.1029/2006jf000470

Kim, W., Paola, C., Voller, V., & Swenson, J. (2006b). Experimental Measurement of the Relative Importance of Controls on Shoreline Migration. *Journal Of Sedimentary Research*, *76*(2), 270-283. doi: 10.2110/jsr.2006.019

Kite, E., Gao, P., Goldblatt, C., Mischna, M., Mayer, D., & Yung, Y. (2017). Methane bursts as a trigger for intermittent lake-forming climates on post-Noachian Mars. *Nature Geoscience*, *10*(10), 737-740. doi: 10.1038/ngeo3033

Kite, E. (2019). Geologic Constraints on Early Mars Climate. *Space Science Reviews*, *215*(1-10). doi: 10.1007/s11214-018-0575-5

Koss, J., Ethridge, F. and Schumm, S. (1994). An Experimental Study of the Effects of Base-Level Change on Fluvial, Coastal Plain and Shelf Systems. *SEPM Journal of Sedimentary Research*, Vol. 10-21

Kraal, E., van Dijk, M., Postma, G. and Kleinhans, M. (2008). Martian stepped-delta formation by rapid water release. *Nature*, 451(7181), 973-976.
Lewis, K. and Aharonson, O. (2006). Stratigraphic analysis of the distributary fan in Eberswalde crater using stereo imagery. *Journal of Geophysical Research*, 111(E6).
Lewis, K., Aharonson, O., Grotzinger, J., Kirk, R., McEwen, A., & Suer, T. (2008). Quasi-Periodic Bedding in the Sedimentary Rock Record of Mars. *Science*, *322*(5907), 1532-1535. doi: 10.1126/science.1161870
Lewis, K. W., O. Aharonson, J. P. Grotzinger, A. S. McEwen, and R. L. Kirk (2010), Global significance of cyclic sedimentary deposits on Mars, Lunar Planet. Sci., XLI, Abstract 2648.
Malin, M., & Carr, M. (1999). Groundwater formation of martian valleys. *Nature*, *397*(6720), 589-591. doi: 10.1038/17551
Malin, M., & Edgett, K. (1999). Oceans or seas in the Martian northern lowlands: High resolution imaging tests of proposed coastlines. *Geophysical Research Letters*, *26*(19), 3049-3052. doi: 10.1029/1999gl002342
Malin, M., & Edgett, K. (2000). Sedimentary Rocks of Early Mars. *Science*, *290*(5498), 1927-1937. doi: 10.1126/science.290.5498.1927
Malin, M. and Edgett, K. (2003). Evidence for Persistent Flow and Aqueous Sedimentation on Early Mars. *Science*, 302(5652), 1931-1934.
Mangold, N., Quantin, C., Ansan, V., Delacourt, C., & Allemand, P. (2004). Evidence for Precipitation on Mars from Dendritic Valleys in the Valles Marineris Area. *Science*, *305*(5680), 78-81. doi: 10.1126/science.1097549
Mangold, N., Kite, E., Kleinhans, M., Newsom, H., Ansan, V., & Hauber, E. et al. (2012). The origin and timing of fluvial activity at Eberswalde crater, Mars. Icarus, 220(2), 530-551. doi: 10.1016/j.icarus.2012.05.026
Martínez, G., & Renno, N. (2013). Water and Brines on Mars: Current Evidence and Implications for MSL. *Space Science Reviews*, *175*(1-4), 29-51. doi: 10.1007/s11214-012-9956-3
Martínez, G., Newman, C., De Vicente-Retortillo, A., Fischer, E., Renno, N., & Richardson, M. et al. (2017). The Modern Near-Surface Martian Climate: A Review of In-situ Meteorological Data from Viking to Curiosity. *Space Science Reviews*, *212*(1-2), 295-338. doi: 10.1007/s11214-017-0360-x
Masursky, H. (1973). An overview of geological results from Mariner 9. *Journal Of Geophysical Research*, *78*(20), 4009-4030. doi: 10.1029/jb078i020p04009
Mitchum, R.M., Jr., and Van Wagoner, J.C. (1991) High-frequency sequences and their stacking patterns: sequence-stratigraphic evidence of high-frequency eustatic cycles. *Sedimentary Geology 70*, 131-160.
Moore, J., Howard, A., Dietrich, W. and Schenk, P. (2003). Martian Layered Fluvial Deposits: Implications for Noachian Climate Scenarios. *Geophysical Research Letters*, 30(24).
Morgan, A., Wilson, S., Howard, A., Craddock, R., Grant, J., (2018). Global distribution of alluvial fans and deltas on Mars, in 49th Lunar and Planetary Science Conference, The Woodlands, Texas. LPI Contribution, vol. 2083, 19-23.
Murray, A., Antonlinez, A., & Mendez, F. (2017). *Autogenic and Allogenic: Emergent Coastline Patterns Interact With Forcing Variations* 1st ed., 50-111.
Muto, T. (2001a). Shoreline Autoretreat Substantiated in Flume Experiments. *Journal of Sedimentary Research*, 71(2), 246-254.

Muto, T. and Steel, R. (2001b). Autostepping during the transgressive growth of deltas: Results from flume experiments. *Geology*, 29(9), 771-780

Muto, T. and Steel, R. (2004). Autogenic response of fluvial deltas to steady sea-level fall: Implications from flume-tank experiments. *Geology*, 32(5), 401-452.

Olsen, H. (1990) Astronomical forcing of meandering river behavior: Milankovitch cycles in Devonian of East Greenland. *Palaeogeography, Palaeoclimatology, Palaeoecology 79*, 99-115.

Olsen, P.E., and Kent, D.V. (1999) Long-period Milankovitch cycles from the Late Triassic and Early Jurassic of eastern North American and their implications for the calibration of the Early Mesozoic time-scale and the long-term behavior of the planets. *Philosophical Transactions: Mathematical, Physical and Engineering Sciences 357* 1761-1786.

Paola, C. (2000). Quantitative models of sedimentary basin filling. *Sedimentology*, *47*, 121-178. doi: 10.1046/j.1365-3091.2000.00006.x

Paola, C., & Voller, V. (2005). A generalized Exner equation for sediment mass balance. *Journal Of Geophysical Research: Earth Surface*, *110*(F4), doi: 10.1029/2004jf000274

Paola, C., Straub, K., Mohrig, D. and Reinhardt, L. (2009). The "unreasonable effectiveness" of stratigraphic and geomorphic experiments. *Earth-Science Reviews*, 97(1-4), 1-43.

Peakall, J., Warburton, J., (1996). Surface tension in small hydraulic river models — the significance of the weber number. *Journal of Hydrology*, 35, 199–212.

Pedocchi, F., & García, M. (2009). Ripple morphology under oscillatory flow: 2. Experiments. *Journal Of Geophysical Research*, *114*(C12). doi: 10.1029/2009jc005356

Pieri, D. (1980). Martian Valleys: Morphology, Distribution, Age, and Origin. *Science*, *210*(4472), 895-897. doi: 10.1126/science.210.4472.895

Pondrelli, M., Rossi, A., Marinangeli, L., Hauber, E., Gwinner, K., Baliva, A. and Di Lorenzo, S. (2008). Evolution and depositional environments of the Eberswalde fan delta, Mars. *Icarus*, 197(2), 429-451.

Pondrelli, M., Rossi, A., Platz, T., Ivanov, A., Marinangeli, L., & Baliva, A. (2011). Geological, geomorphological, facies and allostratigraphic maps of the Eberswalde fan delta. *Planetary And Space Science*, *59*(11-12), 1166-1178. doi: 10.1016/j.pss.2010.10.009

Posamentier, H .W., Jervey, M.T., and Vail, P.R., (1988). Eustatic controls on clastic deposition I--conceptual framework, in Wilgus, C.K., Hastings, B.S., Kendall, C.G.St.C., Posamentier, H.W., Ross, C.A., and Van Wagoner, J.C., eds., Sea Level Change--An Integrated Approach: SEPM Special Publication 42, 110-124.

Posamentier, H. and Allen, G. (1992). High Resolution Sequence Stratigraphy--The East Coulee Delta, Alberta. *SEPM Journal of Sedimentary Research*, 3-28.

Postma, G. (1990) Depositional architecture and facies of river and fan deltas: a synthesis. In: Coarse Grained Deltas (Ed. by A. Collela & D.B. Prior), Int. Ass. Sedimentol. Spec. Publ., 10, 13-27.

Postma, G., Kleinhans, M., Meijer, P., & Eggenhuisen, J. (2008). Sediment transport in analogue flume models compared with real-world sedimentary systems: a new look at scaling evolution of sedimentary systems in a flume. *Sedimentology*, *55*(6), 1541-1557. doi: 10.1111/j.1365-3091.2008.00956.x

Rice, M., Gupta, S., Bell, J., & Warner, N. (2011). Influence of fault-controlled topography on fluvio-deltaic sedimentary systems in Eberswalde crater, Mars. *Geophysical Research Letters*, *38*(16), doi: 10.1029/2011gl048149

Rovere, A., Stocchi, P. and Vacchi, M. (2016) Eustatic and Relative Sea Level Changes. *Current Climate Change Reports 2*, 221-231. doi:10.1007/s40641-016-0045-7

Schon, S., Head, J., & Fassett, C. (2012). An overfilled lacustrine system and progradational delta in Jezero crater, Mars: Implications for Noachian climate. *Planetary And Space Science*, *67*(1), 28-45. doi: 10.1016/j.pss.2012.02.003

Schumm, S., & Lichty, R. (1965). Time, space, and causality in geomorphology. *American Journal Of Science*, *263*(2), 110-119. doi: 10.2475/ajs.263.2.110

Schlager, W. (1993). Accommodation and supply—a dual control on stratigraphic sequences. *Sedimentary Geology*, *86*(1-2), 111-136. doi: 10.1016/0037-0738(93)90136-s

Schwarzacher, W. (2000). Repetitions and cycles in stratigraphy. *Earth-Science Reviews 50*, 51-75.

Sekiguchi, T., & Sunamura, T. (2004). Effects of bed perturbation and velocity asymmetry on ripple initiation: wave-flume experiments. *Coastal Engineering*, *50*(4), 231-239. doi: 10.1016/j.coastaleng.2003.11.002

Straub, K.M., Duller, R.A., Foreman, B.Z., Hajek, E.A. (2020) Buffered, incomplete, and shredded: The challenges of reading an imperfect stratigraphic record. *Journal of Geophysical Research: Earth Surface 125*, e2019JF005079.

Toby, S., Duller, R., De Angelis, S., & Straub, K. (2019). A Stratigraphic Framework for the Preservation and Shredding of Environmental Signals. *Geophysical Research Letters*, *46*(11), 5837-5845. doi: 10.1029/2019gl082555

Vail, P.R., Mitchum, Jr., R.M. (1979) Global cycles of relative changes of sea level from seismic stratigraphy. Geological and Geophysical Investigations of Continental Margins 469-472.

Van Heijst, M. and Postma, G. (2001). Fluvial response to sea-level changes: a quantitative analogue, experimental approach. *Basin Research*, 13(3), 269-292.

Wood, L. (2006). Quantitative geomorphology of the Mars Eberswalde delta. *Geological Society Of America Bulletin*, *118*(5-6), 557-566. doi: 10.1130/b25822.1

Watts, A. (1982). Tectonic subsidence, flexure and global changes of sea level. *Nature*, *297*(5866), 469-474. doi: 10.1038/297469a0

Yalin, M.S., (1971). Theory of hydraulic models. *MacMillan, London*. 266 pp

Zabrusky, K., Andrews-Hanna, J., & Wiseman, S. (2012). Reconstructing the distribution and depositional history of the sedimentary deposits of Arabia Terra, Mars. *Icarus*, *220*(2), 311-330. doi: 10.1016/j.icarus.2012.05.007

Ziberi, B., Frost, F., Höche, T., & Rauschenbach, B. (2005). Ripple pattern formation on silicon surfaces by low-energy ion-beam erosion: Experiment and theory. *Physical Review B*, *72*(23). doi: 10.1103/physrevb.72.235310

Tables and Figures

Tables

Table 1. Experimental run parameters and durations.

Run	Q_w (L/min)	Q_s (L/min)	Basin Volume (Liters)	Run Time (Min)	Spill Time (Min)
1A	0.8	0.13	121	278	226
1B	0.8	0.19	121	214	148
1C	0.8	0.22	121	184	172
2A	0.8	0.13	159	281	145
2B	0.8	0.19	159	195	132

Table 2. Extracted shoreline trajectory data points from interpreted dip cross sections.

Run	Total Points	Average Points per Dip Section
1A	119	5
1B	149	7
1C	60	3
2A	123	6
2B	121	6

Table 3. Coal percentage for each phase and total coal percentage for each Run.

Phase	1A	1B	1C	2A	2B
1	32.2	27.0	31.4	15.2	27.5
2	25.6	17.6	30.2	26.8	12.1
3	22.4	23.5	27.3	27.2	17.6
4	06.0	20.8	32.2	28.3	16.8
5	28.9	11.1	28.0	38.6	19.4
Total	25.0	21.0	29.3	26.2	17.9

Table 4. Flume 1 strike cross sectional area of coal bodies normalized by the coal area of each phase. Also presented is the number of coal bodies within each phase.

Phase	1A Avg	1A Stdv	1A Coal Bodies	1B Avg	1B Stdv	1B Coal Bodies	1C Avg	1C Stdv	1C Coal Bodies
1	3.2	2.4	10	2.1	2.8	13	1.9	2.0	17
2	1.3	0.9	20	1.0	0.6	18	1.9	3.9	16
3	1.5	1.0	15	1.1	2.2	21	1.1	1.8	24
4	0.6	0.4	10	1.0	1.7	21	3.6	4.3	9
5	2.2	3.9	13	0.5	0.9	22	1.3	3.7	21

Table 5. Flume 2 strike cross sectional area of coal bodies normalized by the coal area of each phase. Also presented is the number of coal bodies within each phase.

Phase	2A Avg	2A Stdv	2A Coal Bodies	2B Avg	2B Stdv	2B Coal Bodies
1	0.9	0.8	17	2.5	2.2	11
2	1.6	1.6	17	1.0	0.7	12
3	1.1	1.6	26	0.6	0.6	28
4	4.0	5.7	7	0.7	0.6	25
5	5.5	11.7	7	0.9	0.8	21

Table 6. Flume 1 aspect ratio of bounding ellipse coal bodies. Also presented is the number of coal bodies within each phase.

Phase	1A Avg	1A Stdv	1A Coal Bodies	1B Avg	1B Stdv	1B Coal Bodies	1C Avg	1C Stdv	1C Coal Bodies
1	7.9	4.8	10	5.5	4.3	13	2.8	1.7	17
2	6.6	2.8	20	5.3	3.0	18	3.3	2.8	16
3	7.1	3.5	15	5.6	3.8	21	4.0	2.0	24
4	3.8	2.2	10	4.8	3.1	21	4.5	2.2	9
5	4.4	2.9	13	3.6	2.7	22	3.6	2.5	21

Table 7. Flume 2 aspect ratio of bounding ellipse coal bodies. Also presented is the number of coal bodies within each phase.

Phase	2A Avg	2A Stdv	2A Coal Bodies	2B Avg	2B Stdv	2B Coal Bodies
1	5.5	3.1	17	4.9	4.0	11
2	6.1	5.0	17	7.0	3.8	12
3	5.8	3.6	26	6.9	3.4	28
4	3.9	1.6	7	4.4	2.0	25
5	4.2	2.6	7	4.2	1.8	21

Table 8. Predicted martian deltaic facies with associated lithologies and sedimentary structures.

Facies	Lithology	Structures
Fluvial	Fine grained conglomerate - coarse grained sandstone Flat lying, fining upward	Medium - small scale uni-directional planar/ trough cross-bedding Planar laminations Scouring Erosional contacts
Delta Plain	Tabular coarse - medium grained sandstone Normal grading, gently inclined beds to the angle of repose Lenticular mudstone Basal imbricated conglomerate	Large scale uni-directional planar/ trough cross-bedding Uni-directional ripples Laminated Basal erosional contact
Delta Front	Fine - very fine grained sandstone Normal grading, steeply inclined beds Interbedded siltstones	Planar laminations Gradational/ diffuse contact Alternating bed thicknesses
Prodelta	Large - medium scale turbidites Interbedded mudstones	Basal scouring, slumping Laminated
Shallow Lacustriane	Very fine grained sandstone Interbedded mudstones Interbedded Evaporites (Ca, Mg, Fe - Sulfate, NaCl)	Thin alternating bed Finely laminated
Deep Lacustriane	Small scale turbidites Interbedded mudstones	Thin alternating bed Finely laminated
Playa	Mudstone Interbedded Evaporites (Ca, Mg, Fe - Sulfate, NaCl)	Mud cracks Thin alternating bed

Figures

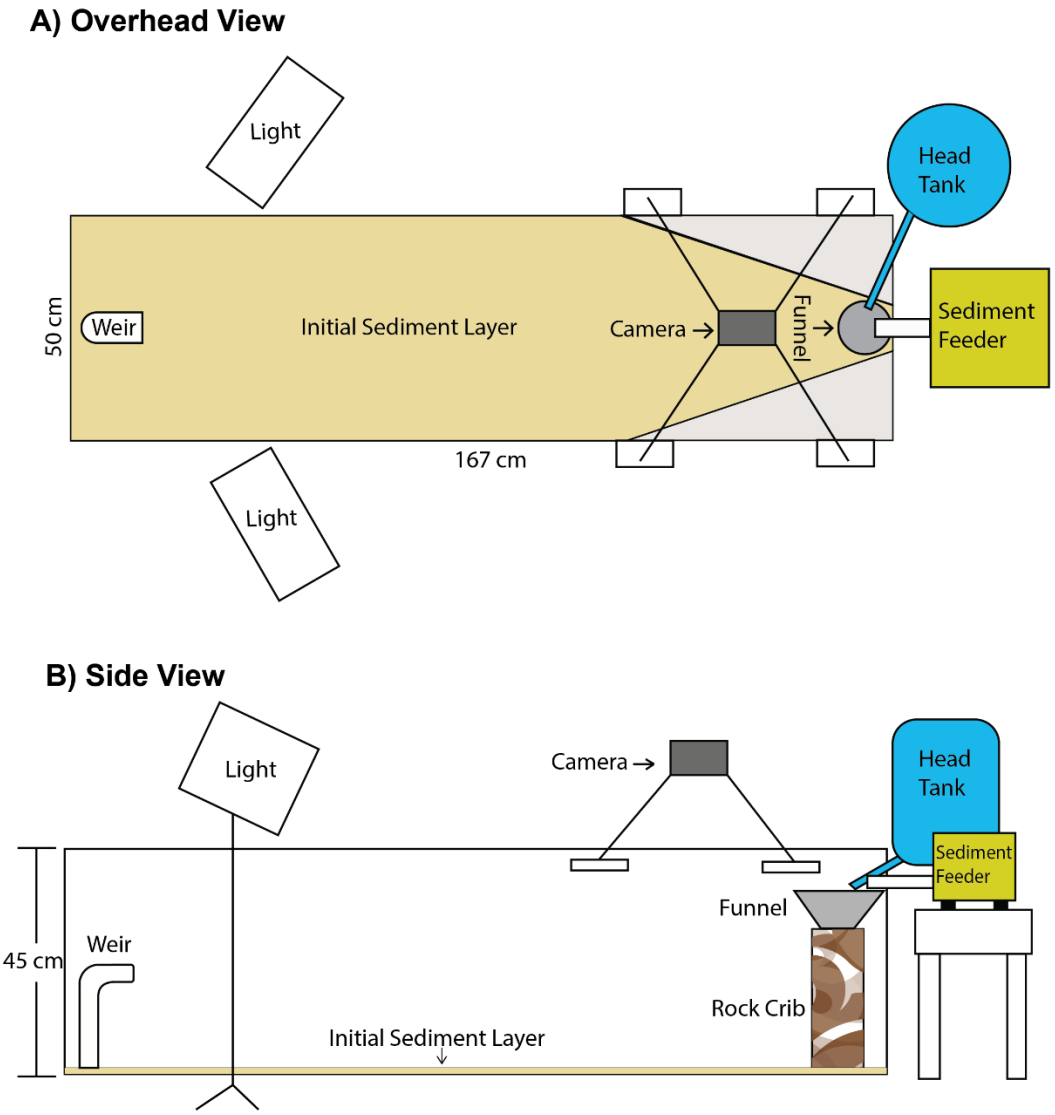

Figure 1. Schematic diagram of the initial experimental conditions for all flume experiments. A) The overhead view and B) the side view.

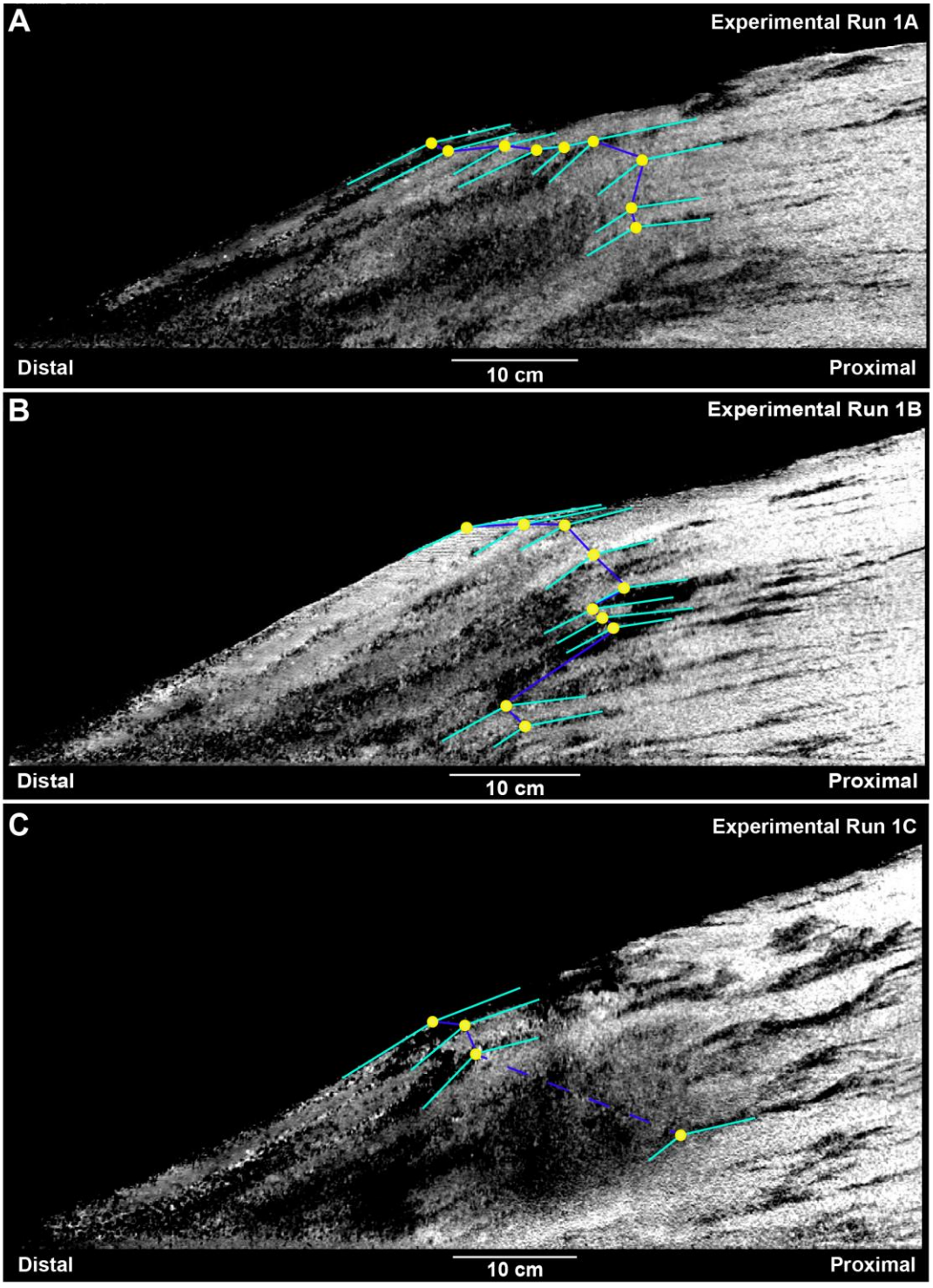

Figure 2. Flume 1 experimental A) Run 1A, B) Run 1B, and C) Run 1C dip cross-sections of shoreline trajectory phases. Traced on each is shoreline data points (yellow circles), the topset to foreset outlines of each associated shoreline (light blue), and the projected shoreline trajectory curve (dark blue). The white colored sediment represents the silica sand and the black colored sediment represents the anthracite coal.

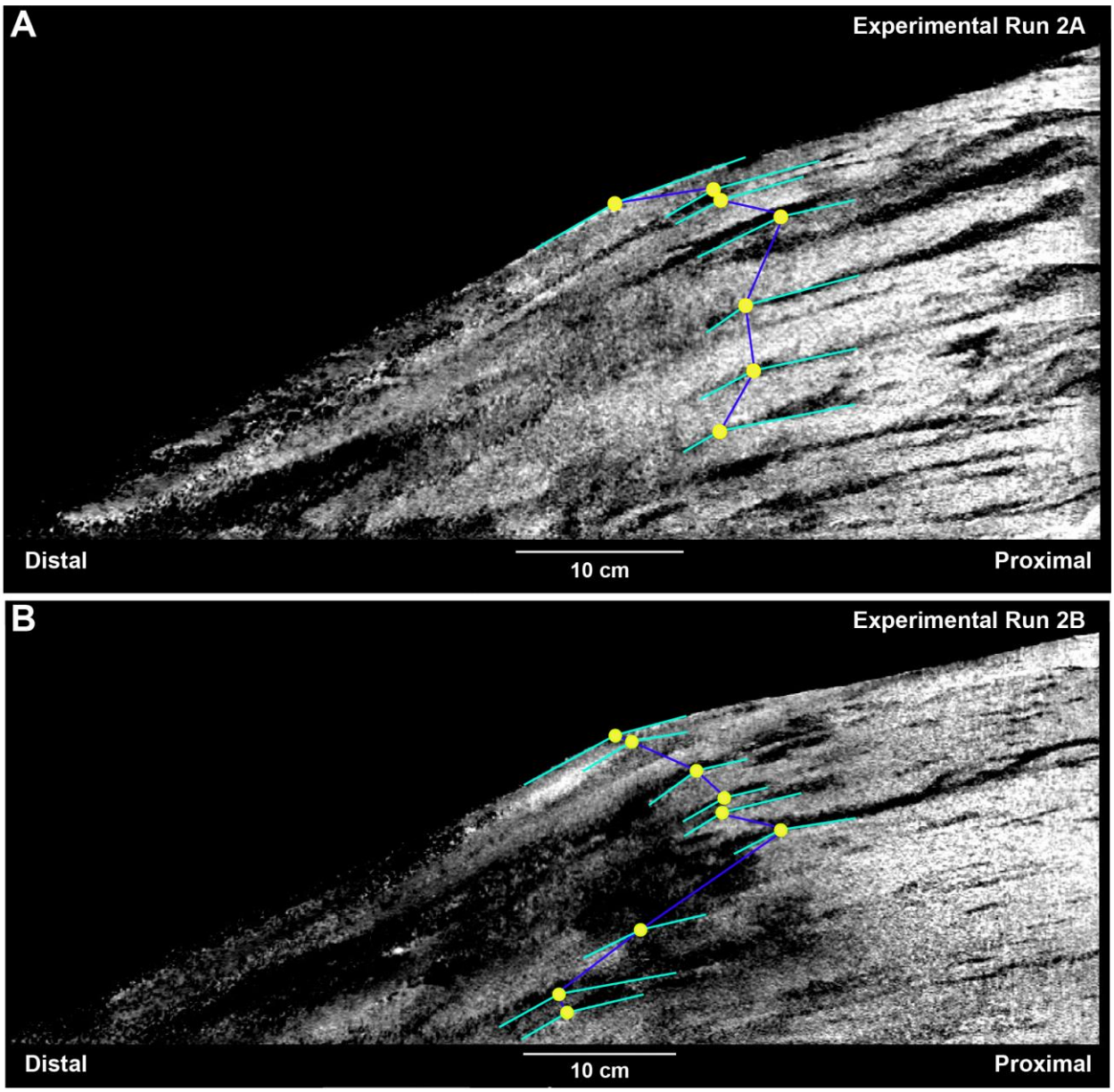

Figure 3. Flume 2 experimental A) Run 2A, and B) Run 2B dip cross-sections of shoreline trajectory phases. Traced on each is shoreline data points (yellow circles), the topset to foreset outlines of each associated shoreline (light blue), and the projected shoreline trajectory curve (dark blue). The white colored sediment represents the silica sand and the black colored sediment represents the anthracite coal.

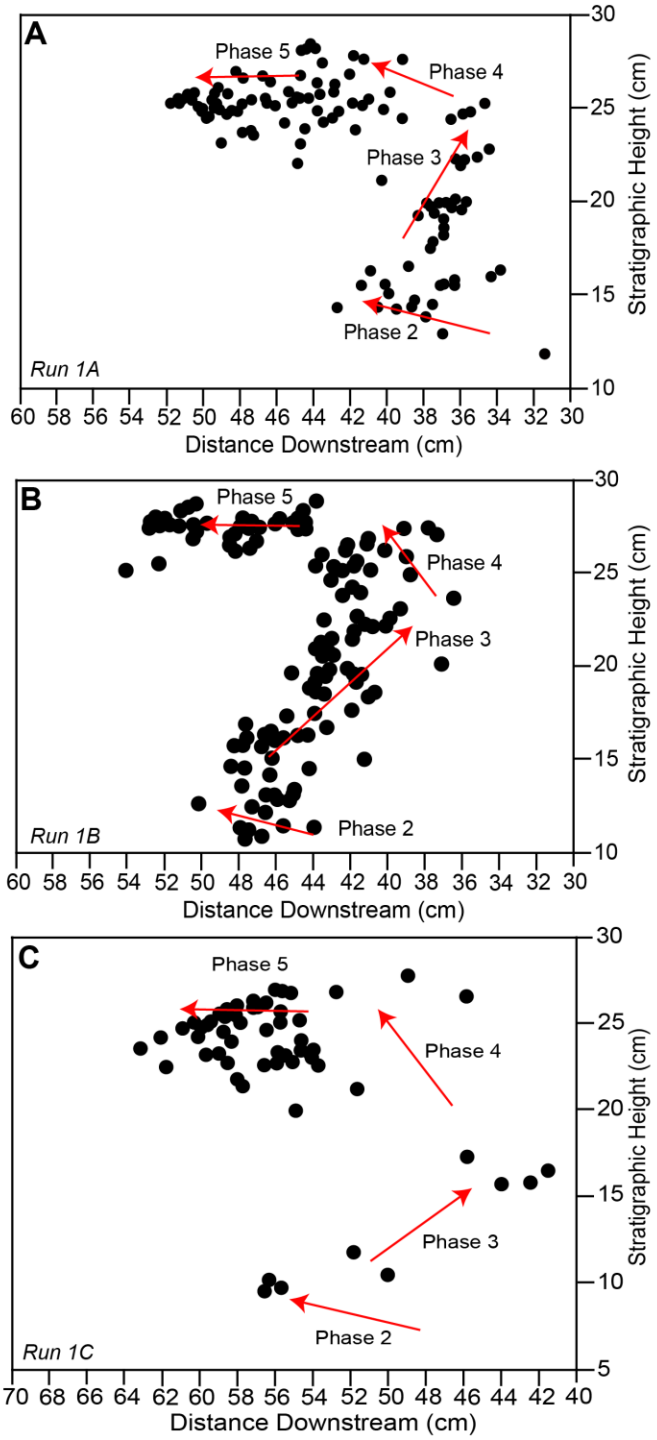

Figure 5. Flume 1: Run 1A (A) and Run 1B (B) and Run 1C (C) complied "stack" of shoreline trajectory data. Associated shoreline trajectory phases labeled with shoreline shift (red arrows).

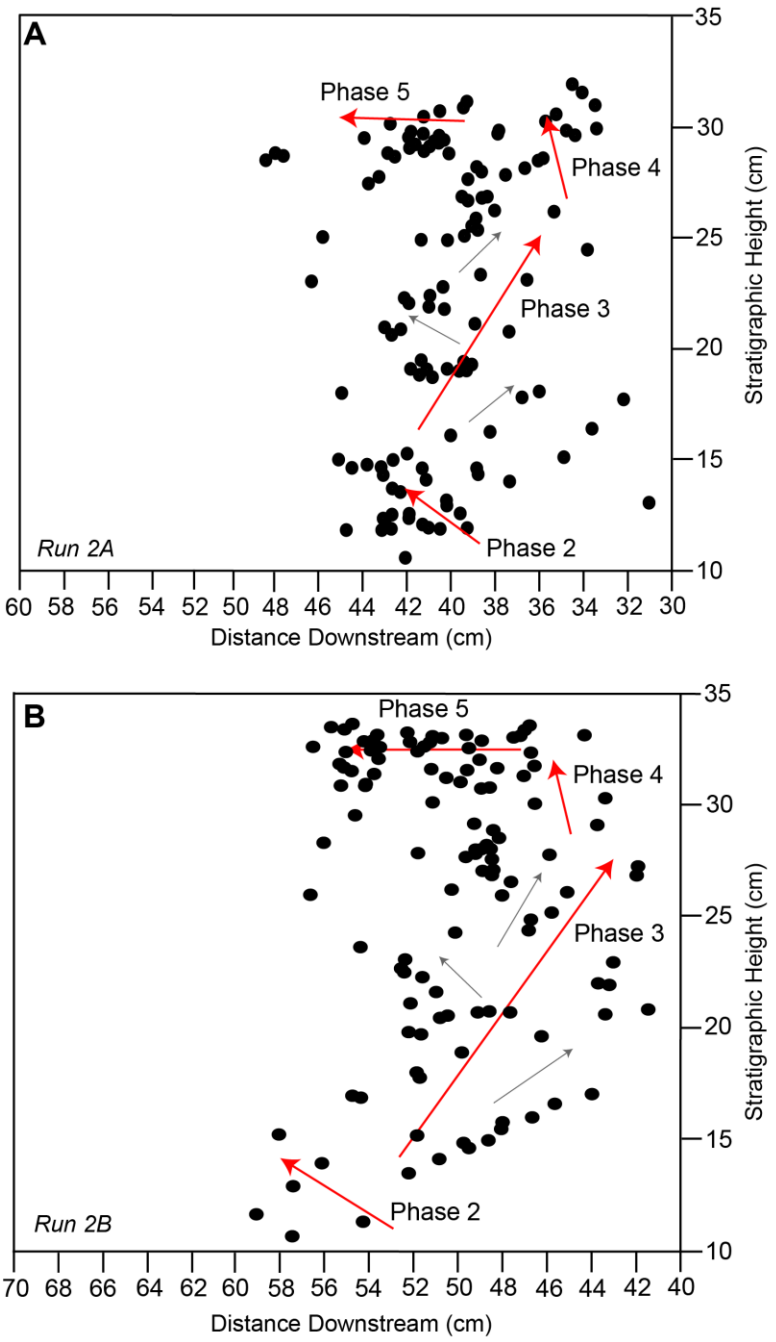

Figure 5. Flume 2: Run 2A (A) and Run 2B (B) complied "stack" of shoreline trajectory data. Associated shoreline trajectory phases labeled with shoreline shift (red arrows), with small scale microphases shoreline shifts (grey arrows).

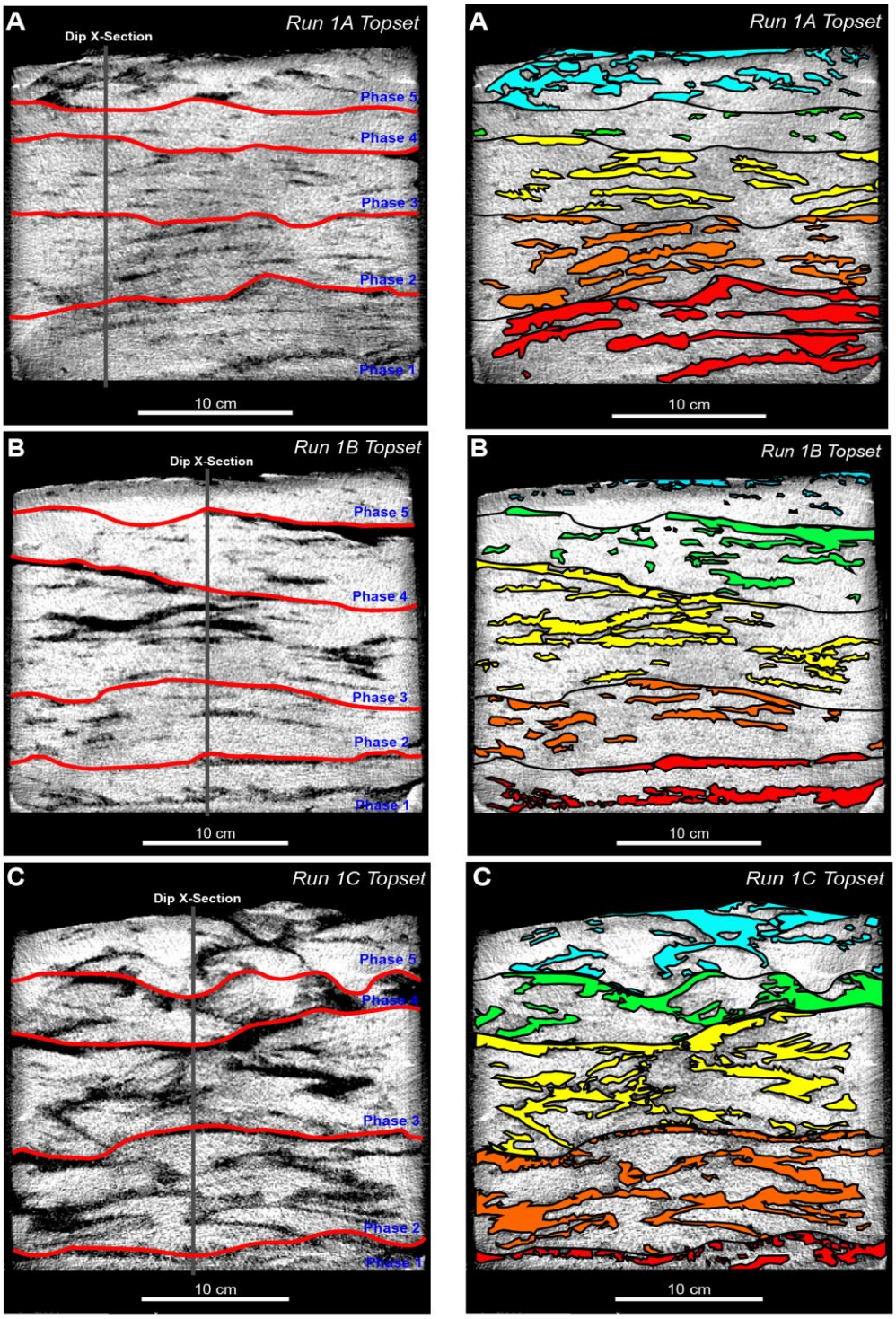

Figure 7. Flume 1: Run 1A (A), Run 1B (B) and Run 1C (C) with original uninterrupted strike cross-section through delta topset location and associated phases (left, blue) phase contacts (left, red), and Figure 3 dip cross-section location (left, grey). The right shows the interrupted strike cross-section with traced anthracite coal deposits for each phase.

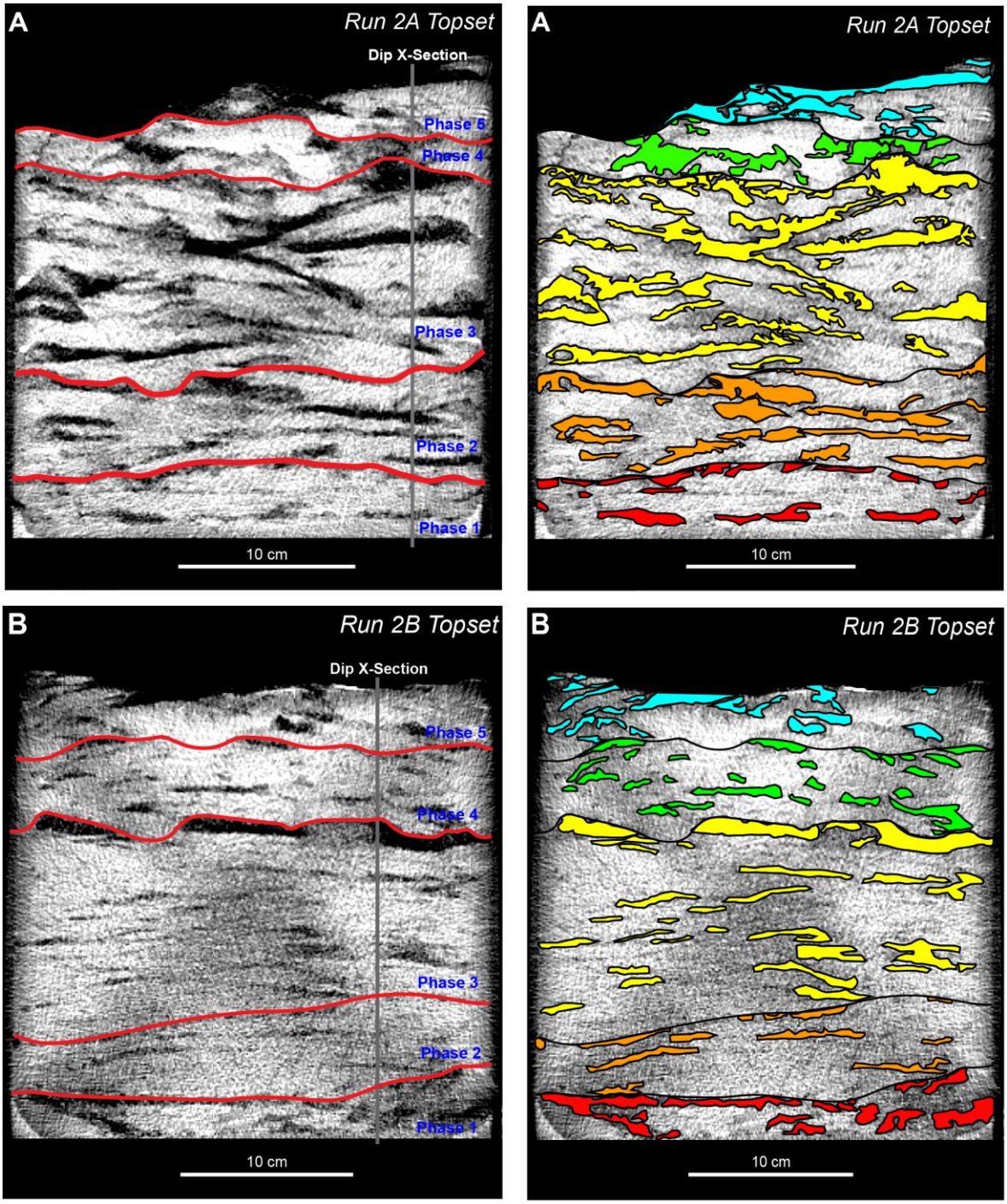

Figure 7. Flume 2: Run 2A (A) and Run 2B (B) with original uninterrupted strike cross-section through delta topset location and associated phases (left, blue) phase contacts (left, red), and Figure 3 dip cross-section location (left, grey). The right shows the interrupted strike cross-section with traced anthracite coal deposits for each phase.

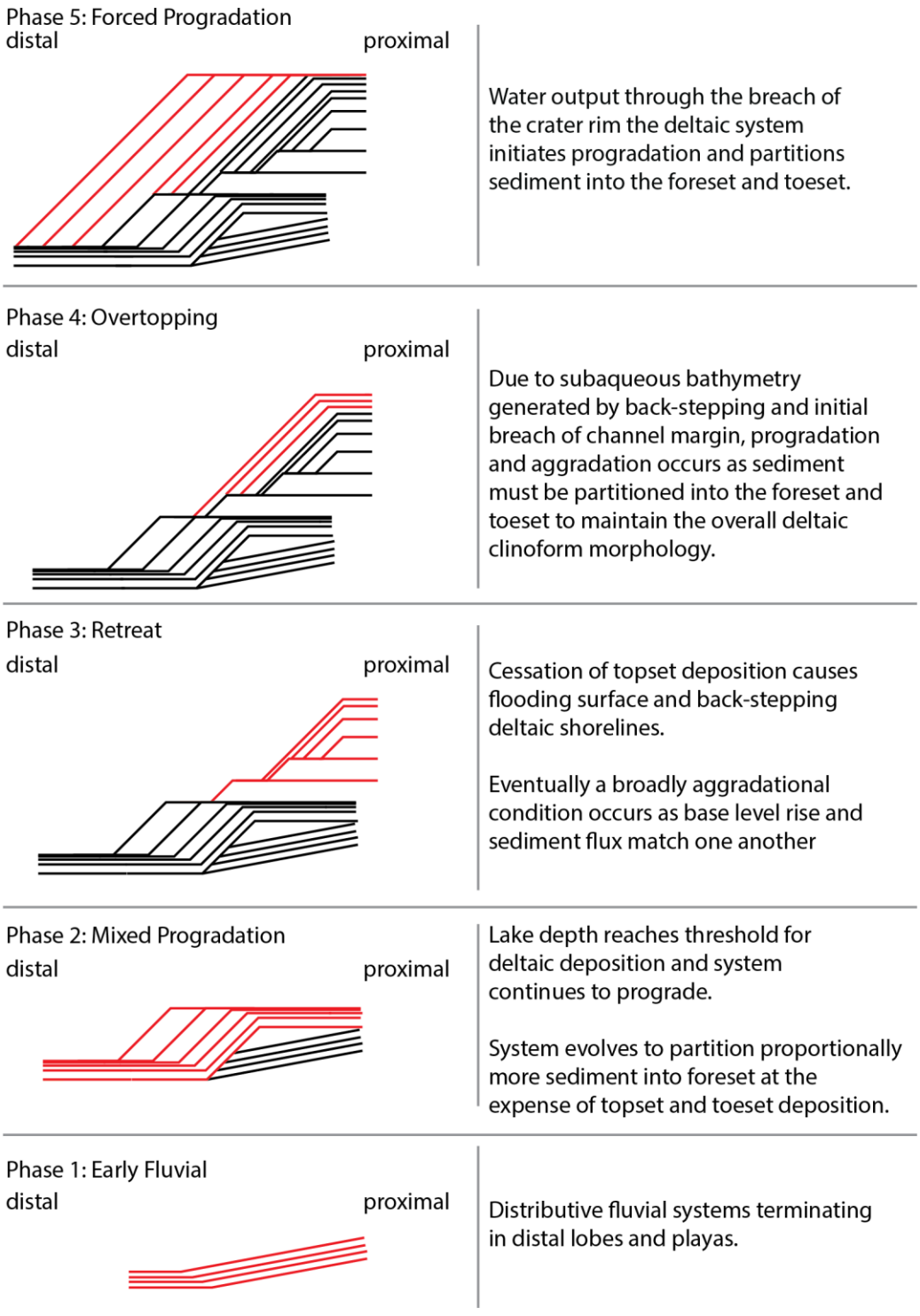

Figure 8. Simplified schematic representation of the produced stratigraphic sequence phases from all experimental runs. Phases one through five are shown with current phase deposition (red) and previous deposits (black) represented.

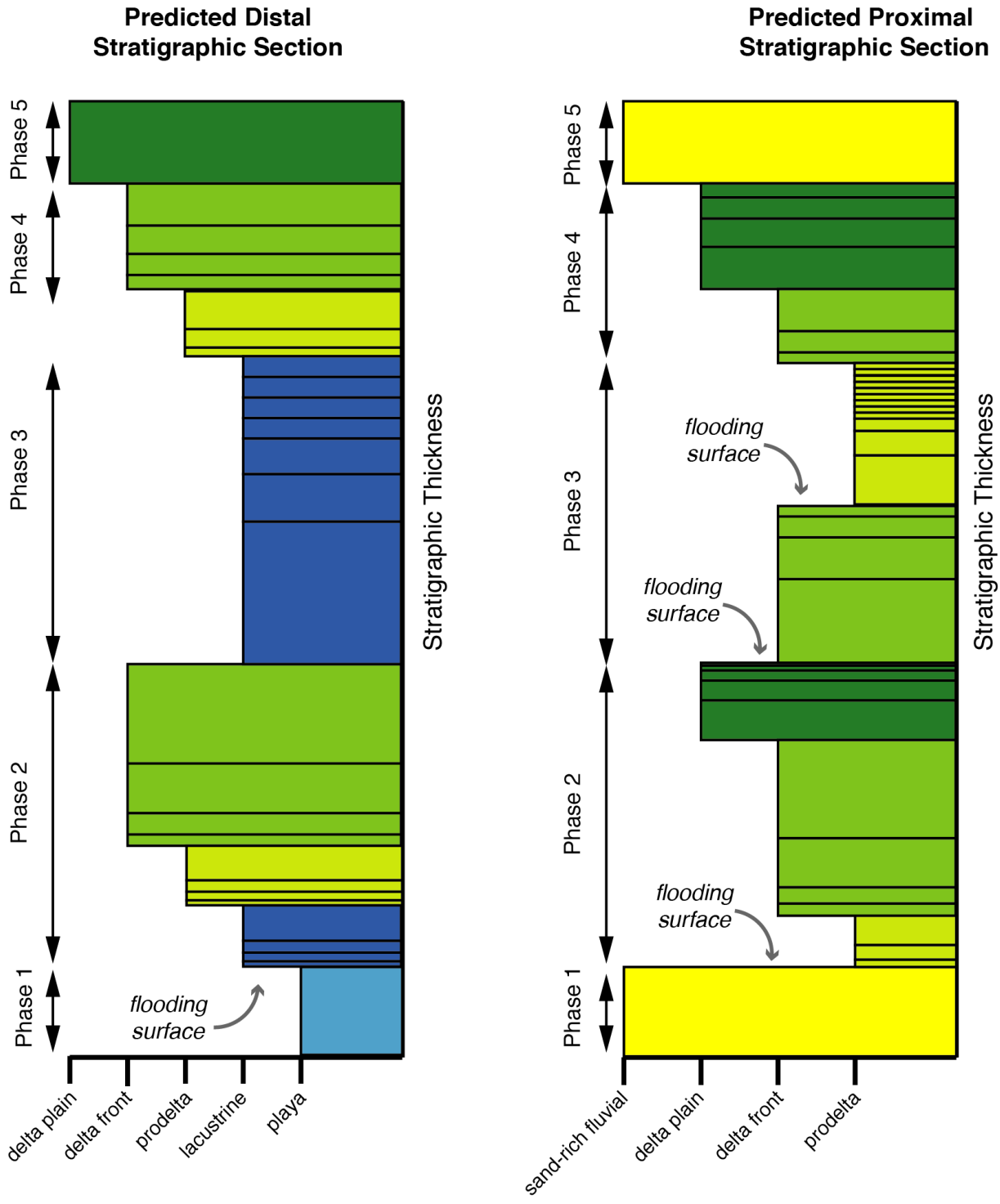

Figure 9. Predicted crater-fill Martian stratigraphic sequence facies separated by the proximal (right) and distal (left) locations. Associated bed thickness, lithofacies and sedimentary structure descriptions seen in Table 8.

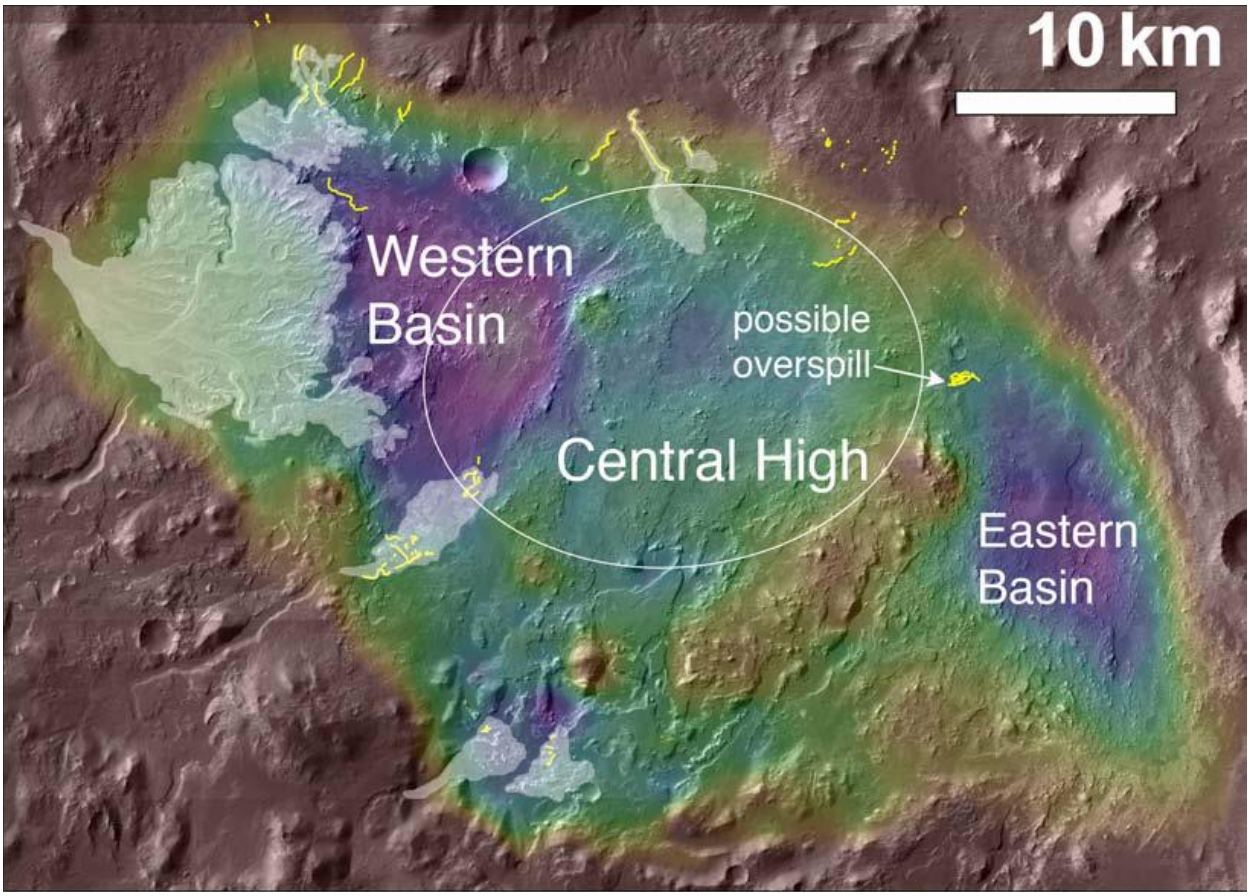

Figure 10. Eberswalde crater division of the Western and Eastern basins with six sedimentary deposits highlighted within the Western basin. Adapted from Rice et al. (2011).

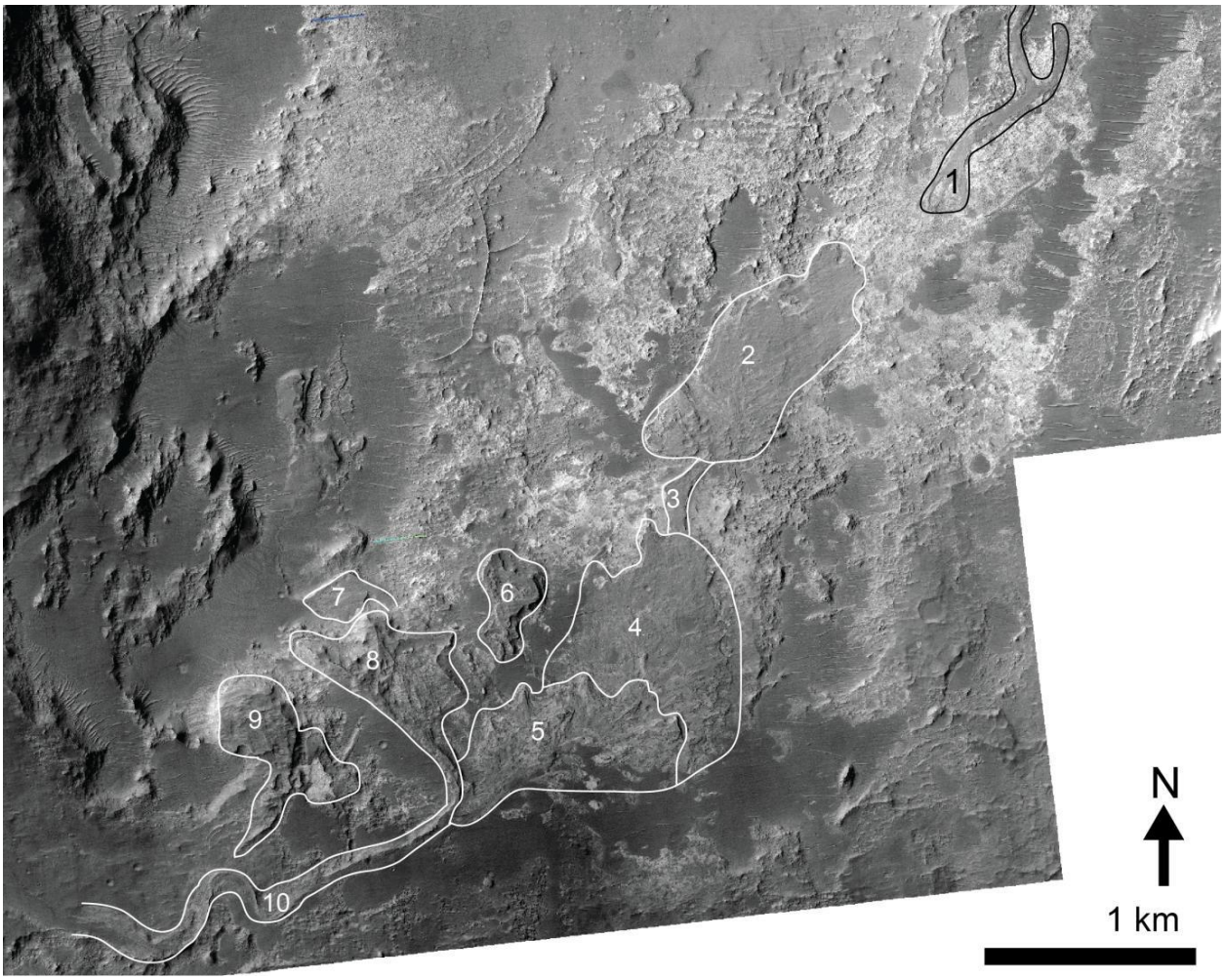

Figure 11. Interpreted identification of ten stratal unit sedimentary deposits making up the Southwest Eberswalde Deposit within the Western basin of Eberswalde Crater. Adapted from Goddard et al. (2013).

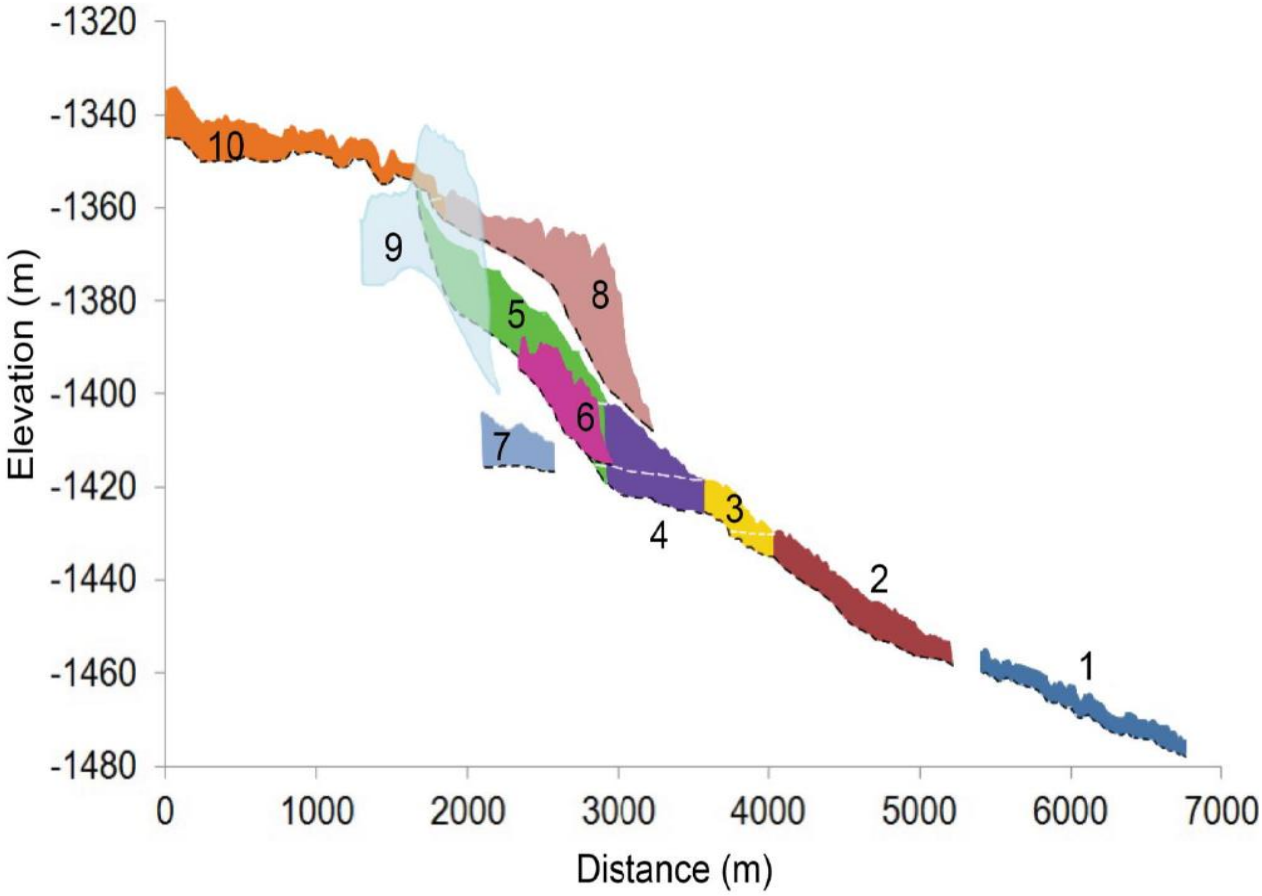

Figure 12. Cross- sectional representation of approximate thickness, straight line distance, and predicted elevation of the Southwest Eberswalde Deposit's ten stratal units. Adapted from Goddard et al. (2013).

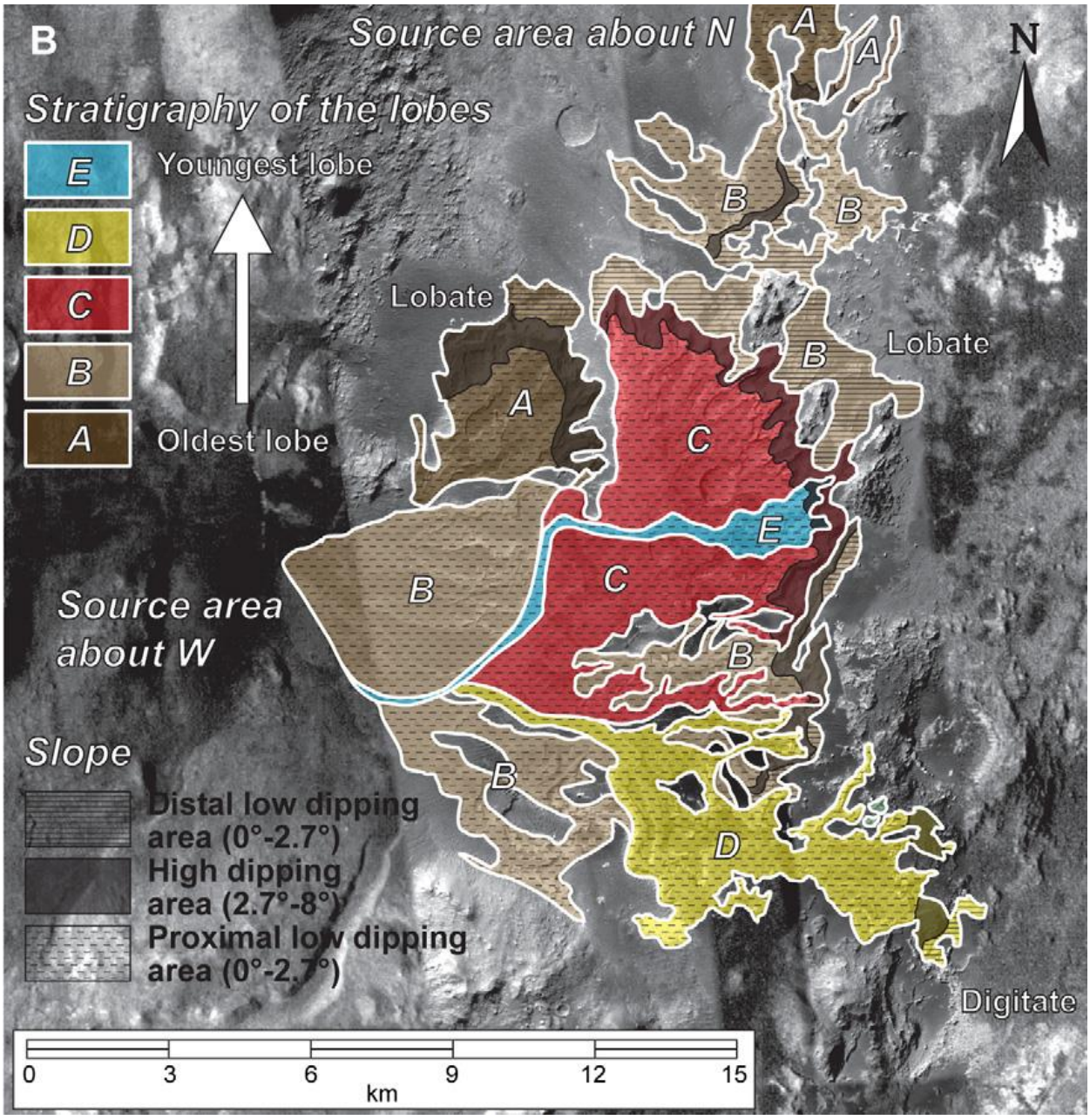

Figure 13. Interpreted outline of Eberswalde Delta lobate features with chronology of lobes represented by color scheme. Adapted from Pondrelli et al. (2008).

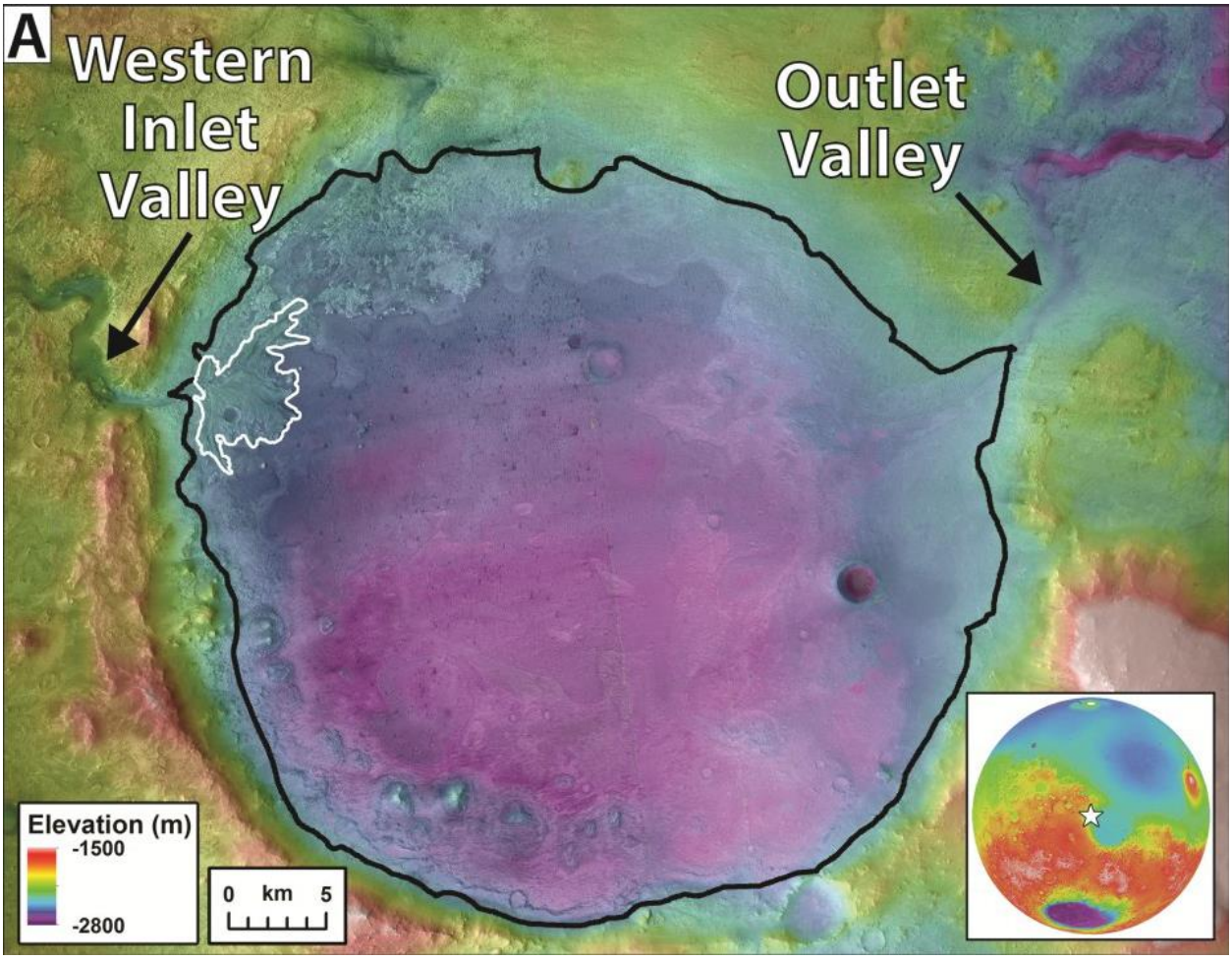

Figure 14. Elevation map of Jezero crater with outlined location of Jezero Western Delta and crater inlet and outlet valleys. Adapted from Goudge et al. (2018).

Appendix A

Overhead video footage of 5 experimental runs:

Experimental Run 1A delta growth video recording

Experimental Run 1B delta growth video recording

Experimental Run 1C delta growth video recording

Experimental Run 2A delta growth video recording

Experimental Run 2B delta growth video recording

Full CT scan of 5 experimental runs:

Experimental Run 1A CT scan data

Experimental Run 1B CT scan data

Experimental Run 1C CT scan data

Experimental Run 2A CT scan data

Experimental Run 2B CT scan data

Appendix B

Experimental Run 1A extracted 3pt running average shoreline data

Slice #	X	Y
214	54.9	12.1
295_I	53.4	12.6
196	50.0	13.3
205_I	47.6	13.6
304_I	46.5	13.8
214	46.9	13.8
196	49.0	13.9
187	49.8	14.0
277_I	49.3	14.2
250	47.7	14.5
295	48.3	14.7
232	49.8	14.8
205	50.3	14.9
286	50.4	14.9
241	50.4	15.0
142	52.8	15.1
151	51.2	15.3
322_I	52.2	15.5
223	50.3	15.6
268	51.7	16.0
169	50.2	16.4
142	51.0	16.9
160	51.3	17.2
187	51.5	17.6
241_I	50.9	17.9
151_I	50.7	18.1
196	51.1	18.2
250	51.9	18.4
223	51.8	18.5
160	51.5	18.6
214	50.9	18.6
142_I	51.1	18.7
169	51.1	18.7
187	52.0	18.7
232	52.3	18.8
205_I	50.9	19.1
232_I	50.7	19.7
205_I	47.1	20.3
187_I	49.0	20.6
187	48.9	20.7
214_I	53.0	20.8
223	53.6	20.9
169_I	50.0	21.2

Slice #	X	Y
205	44.2	21.4
196	38.9	21.6
313	37.6	21.8
151	38.3	22.0
223_I	40.6	22.1
232_I	42.0	22.1
151	42.7	22.2
169	42.0	22.4
214_I	45.3	22.5
160_I	48.0	22.6
142_I	45.4	22.7
142	42.7	22.7
142	38.3	22.7
151	38.7	22.8
187_I	41.7	22.8
223_I	47.6	22.9
214	47.9	22.9
277	45.0	23.0
322_I	39.0	23.0
295	38.2	23.0
169	37.7	23.0
160	38.3	23.0
214	42.5	23.0
241_I	40.2	23.1
277	39.5	23.1
322	35.4	23.1
304_I	35.3	23.1
160	35.2	23.2
196	38.9	23.2
277	40.3	23.3
160	40.7	23.3
286	38.0	23.3
286	35.6	23.3
169	41.7	23.3
196_I	44.2	23.4
160	44.4	23.4
160	39.4	23.4
187_I	38.1	23.4
205_I	38.8	23.4
313	37.1	23.5
277	34.6	23.5
322	35.5	23.5
223	39.5	23.5

Slice #	X	Y
169	39.4	23.6
304	39.7	23.6
205	38.4	23.6
187_I	38.6	23.6
295	39.4	23.6
286	39.1	23.6
142_I	39.1	23.7
286	36.7	23.7
313	37.2	23.8
322	37.8	23.8
223	38.6	23.8
187	35.7	23.8
151	39.7	23.9
160	42.1	23.9
304_I	44.3	23.9
277	40.4	24.0
268	40.4	24.1
295_I	41.1	24.2
268	42.2	24.3
268_I	40.2	24.4
214	38.9	24.5
205	39.6	24.6
268	42.0	24.7
232	41.4	24.7
142	41.9	24.9
259	43.1	25.2
286_I	46.0	25.4
241	46.7	25.5
250	44.4	25.6
259	43.1	25.8
241	42.2	25.9
232	42.4	26.0
250	42.6	26.0

Experimental Run 1B extracted 3pt running average shoreline data

Slice #	X	Y
208_I	-48.8	10.7
199_I	-47.8	10.8
235	-48.6	11.1
172_I	-44.8	11.2
280	-49.1	11.3
262	-46.6	11.3
181	-46.6	11.4
154_I	-47.6	12.0
181	-48.4	12.3
235	-51.5	12.5
199_I	-46.3	12.7
298	-46.9	12.7
172	-47.1	12.9
163	-46.1	12.9
271_I	-47.6	13.0
262	-46.0	13.2
298_I	-49.0	13.4
208_I	-47.4	14.0
217	-45.1	14.3
244	-48.8	14.4
163_I	-49.6	14.4
199	-41.9	14.8
181	-47.2	14.9
271_I	-47.8	15.5
253	-49.4	15.5
190	-48.9	15.6
280	-47.1	15.8
289	-46.6	15.9
208	-48.7	15.9
325	-45.7	16.0
316	-45.2	16.1
226	-47.6	16.1
217	-47.6	16.1
199	-47.3	16.2
307	-44.1	16.5
289_I	-48.7	16.6
154	-46.4	17.0
163	-44.8	17.2
262	-42.6	17.3
244_I	-42.7	17.4
217	-41.7	18.1
172	-41.4	18.3
271	-44.3	18.3

Slice #	X	Y
280_I	-44.6	18.3
298_I	-45.0	18.3
316	-45.1	18.5
325	-44.8	18.8
235	-42.4	18.9
280	-44.8	19.1
262	-44.2	19.2
226	-42.1	19.3
271_I	-44.6	19.3
244	-42.6	19.3
298_I	-46.2	19.3
235	-44.0	19.5
307	-42.9	19.5
217	-37.5	19.8
289	-44.4	20.2
244	-43.8	20.3
235	-44.0	20.5
316_I	-44.7	20.6
181_I	-44.7	20.8
190	-44.5	20.8
172_I	-44.4	20.9
208_I	-42.7	21.1
217	-43.8	21.1
280_I	-42.5	21.5
271	-41.6	21.8
262_I	-41.4	21.8
253	-40.7	21.8
235	-42.0	21.8
190	-44.2	22.1
226	-40.5	22.1
154_I	-42.4	22.3
163	-39.9	22.7
307_I	-36.8	23.2
253_I	-43.2	23.4
325	-42.2	23.5
307	-42.1	23.6
226_I	-42.6	23.8
244_I	-43.9	24.2
289_I	-39.3	24.5
181	-55.6	24.7
217	-43.2	24.7
154	-41.6	24.7
235	-43.8	24.8

Slice #	X	Y
190	-43.6	24.9
172_I	-42.5	24.9
154	-44.7	24.9
172	-53.7	25.0
181_I	-42.4	25.1
316_I	-39.5	25.4
199	-44.4	25.5
163	-49.4	25.7
163_I	-40.7	25.7
208	-42.9	25.8
172	-43.0	25.8
172	-48.5	25.9
181	-42.9	25.9
154	-49.7	26.0
226	-41.8	26.1
181	-48.1	26.2
163	-41.7	26.3
190	-51.8	26.3
298	-49.7	26.4
163	-49.4	26.5
271	-37.8	26.6
199	-51.6	26.7
325	-45.4	26.8
253	-45.7	26.8
217	-39.7	26.9
244	-45.8	26.9
262	-38.3	26.9
280	-47.9	26.9
253	-54.3	26.9
253	-48.9	26.9
244	-49.1	26.9
271	-48.3	26.9
316	-45.3	27.0
280	-45.3	27.0
226	-52.6	27.0
199	-48.3	27.0
217	-51.8	27.0
244	-53.7	27.1
217	-49.0	27.1
262	-45.2	27.1
235	-53.2	27.1
325	-54.3	27.1
280	-48.6	27.1

Slice #	X	Y
208	-51.0	27.1
271	-45.3	27.2
235_I	-46.1	27.2
325	-47.1	27.2
262	-48.6	27.2
226	-48.5	27.2
208	-48.4	27.2
199	-45.9	27.3
190_I	-45.7	27.3
271	-53.6	27.3
262	-53.5	27.3
316	-46.8	27.3
235	-48.9	27.4
307	-54.0	27.4
298	-52.5	27.8
307_I	-45.5	27.8
280	-51.9	28.0
289	-52.0	28.1
316	-51.6	28.1
289	-44.7	28.3

Experimental Run 1C extracted 3pt running average shoreline data

Slice #	X	Y
296_I	-57.1	10.0
287_I	-56.7	10.2
332	-54.4	10.5
143_I	-53.1	11.2
323	-48.8	13.1
233	-46.2	14.9
224_I	-42.7	16.5
242	-43.3	17.0
314	-47.6	18.5
269	-51.1	20.1
305	-55.2	21.5
215_I	-56.3	22.1
224_I	-59.8	22.5
242	-58.4	22.9
179	-57.9	23.2
287_I	-55.9	23.3
296_I	-57.6	23.3
179	-57.0	23.4
143	-56.4	23.5
197	-55.4	23.6
305_I	-55.5	23.7
161	-57.4	23.8
215	-58.6	23.8
197	-58.8	23.9
170	-56.9	24.0
332	-55.2	24.0
323	-54.7	24.1
314_I	-57.8	24.1
215	-59.3	24.3
206	-59.3	24.5
206	-58.9	24.7
242	-59.6	24.8
287	-61.0	25.0
224	-59.0	25.1
143	-59.3	25.3
224	-59.7	25.4
206	-60.8	25.5
179	-60.6	25.6
323	-59.9	25.7
170	-58.5	25.7
152	-58.2	25.8
197	-57.1	25.8
188	-58.1	25.9

Slice #	X	Y
188	-57.7	26.1
161	-59.2	26.2
233	-58.2	26.3
233	-58.3	26.4
314	-57.7	26.5
170	-58.2	26.6
152	-57.6	26.7
251	-57.9	26.7
305	-57.7	26.8
143	-57.8	26.9
278	-53.6	27.1
278_I	-53.1	27.3
260	-51.6	27.4
269	-55.0	27.5
332	-55.3	27.6
296	-53.9	27.9
278_I	-52.8	28.1

Experimental Run 2A extracted 3pt running average shoreline data

Slice #	X	Y
229	-43.5	10.2
220_I	-42.5	10.4
175	-42.7	10.9
193	-42.2	10.9
211	-41.8	10.9
157	-41.2	10.9
166	-40.6	11.0
202	-41.8	11.1
292	-42.1	11.3
229	-42.3	11.4
247	-42.2	11.5
184	-41.4	11.5
148	-40.8	11.7
274	-37.0	11.9
319	-37.2	12.1
283	-37.9	12.3
229	-41.8	12.5
193_I	-40.8	12.8
319	-40.4	13.0
211_I	-40.6	13.1
175	-41.0	13.3
238_I	-40.3	13.4
220_I	-39.7	13.5
184	-41.6	13.6
274	-43.0	13.6
256	-43.8	13.7
283	-43.2	13.8
265	-43.9	13.9
292	-40.9	14.1
301_I	-40.7	14.2
328	-39.0	14.5
310	-40.1	14.9
319	-37.3	15.3
157	-34.7	15.8
220_I	-34.2	16.3
301_I	-38.0	16.9
220_I	-39.3	17.0
157	-40.7	17.3
274	-39.5	17.6
292	-40.7	17.9
328	-40.1	18.0
319	-40.3	18.1
229	-40.8	18.1

Slice #	X	Y
238_I	-41.1	18.1
283	-40.1	18.2
310	-39.6	18.3
265	-40.0	18.4
184	-41.2	18.9
247	-40.5	19.3
157	-40.8	19.8
238_I	-40.9	19.9
220	-41.4	20.0
301	-40.8	20.3
229	-40.1	20.6
274	-40.8	20.9
202	-41.3	21.0
283	-41.7	21.2
310	-41.7	21.3
328	-41.2	21.6
148	-42.6	21.8
238_I	-41.1	22.0
211	-40.5	22.2
256	-36.4	22.7
193	-37.6	23.3
274	-38.5	23.8
202	-42.5	24.0
283	-42.2	24.1
256	-41.4	24.3
265	-39.1	24.4
310	-39.0	24.7
319	-37.8	24.9
166	-37.5	25.2
301	-37.6	25.5
202	-38.7	25.7
292	-38.8	25.9
211	-38.8	25.9
184	-40.6	26.1
256	-40.9	26.4
328	-42.1	26.7
247	-40.0	26.8
193	-39.9	26.9
319	-37.6	27.1
175	-38.1	27.2
310	-37.2	27.3
157	-41.1	27.5
319	-40.1	27.6

Slice #	X	Y
166	-42.3	27.7
265	-42.0	27.7
310	-43.5	27.8
184	-43.5	27.8
256	-43.7	27.9
328	-44.0	27.9
166	-43.7	28.0
247	-41.4	28.1
283	-41.6	28.2
238	-41.5	28.2
328	-41.5	28.3
274	-41.1	28.3
292	-40.8	28.4
184	-40.6	28.4
175	-41.0	28.5
319	-41.4	28.6
274	-42.6	28.6
283	-42.2	28.6
229	-39.6	28.7
211_I	-38.9	28.7
292	-39.2	28.7
283	-40.4	28.8
157	-40.4	28.8
328	-39.2	28.9
148	-38.2	28.9
148	-35.4	29.0
220_I	-37.0	29.1
301_I	-37.3	29.2
202	-39.9	29.4
274	-37.4	29.5
193	-39.0	29.7
247	-38.4	29.8
229	-37.8	30.0
211_I	-37.4	30.1
238	-35.6	30.3
211	-36.0	30.6
220	-34.3	30.8

Experimental Run 2B extracted 3pt running average shoreline data

Slice #	X	Y
305_I	-57.1	10.9
289_I	-58.3	11.1
305	-58.2	11.7
153_I	-57.5	12.3
233_I	-56.4	12.9
145	-54.0	13.3
177_I	-53.1	13.6
249	-50.8	13.8
193	-50.0	14.0
257	-50.8	14.2
193	-53.8	14.3
153_I	-53.6	14.4
201_I	-52.2	14.6
209	-48.1	14.8
169	-47.2	15.1
217	-49.5	15.4
305_I	-52.5	15.7
145	-51.9	15.8
185_I	-50.9	16.0
177_I	-49.8	16.3
225	-52.0	16.8
241_I	-50.0	17.3
161	-49.9	17.8
233_I	-50.7	18.1
281	-52.4	18.3
273_I	-52.0	18.5
265	-48.8	18.7
185_I	-47.6	18.8
209	-47.1	18.8
241_I	-49.0	18.9
249	-46.8	18.9
169	-47.9	19.0
233	-48.7	19.3
225	-49.4	19.6
185_I	-46.3	19.8
193_I	-46.5	20.0
281	-49.9	20.2
273_I	-53.1	20.4
145	-50.0	20.5
217_I	-50.0	20.7
265_I	-50.6	20.9
257_I	-53.2	21.3
249_I	-51.2	21.7

Slice #	X	Y
297	-48.5	21.9
289	-47.2	22.0
305	-46.8	22.2
313	-47.3	22.7
225	-50.9	23.0
153	-50.6	23.2
201_I	-51.4	23.3
273	-48.1	23.4
281	-47.0	23.6
161	-46.4	23.8
305	-46.8	24.0
249	-49.2	24.0
257_I	-46.8	24.1
217_I	-46.7	24.3
225	-47.1	24.4
297	-48.5	24.6
313	-49.7	24.7
145_I	-49.6	24.7
305	-50.6	24.8
201	-49.6	24.8
289	-49.5	24.9
313	-49.6	24.9
281	-52.0	25.0
153	-51.8	25.1
249	-51.7	25.3
241	-47.2	25.5
217_I	-47.6	25.7
185	-49.9	25.9
265_I	-50.9	26.2
193_I	-51.5	26.4
305	-47.4	26.6
161	-48.3	26.8
241	-47.4	27.0
281	-51.7	27.1
265_I	-53.6	27.2
153	-55.6	27.2
177	-53.7	27.3
297	-52.3	27.4
145_I	-49.8	27.5
249_I	-51.2	27.5
225	-52.7	27.6
145	-53.6	27.7
289	-52.7	27.8

Slice #	X	Y
185	-50.4	27.8
313	-52.4	27.8
177	-50.7	27.9
273	-53.3	27.9
145	-51.0	28.0
281	-53.6	28.1
201	-50.5	28.2
193	-52.6	28.3
305	-52.0	28.4
233	-54.6	28.5
217	-54.1	28.5
185	-53.2	28.6
217	-54.2	28.6
289	-53.5	28.6
209	-54.4	28.7
169	-53.6	28.8
225	-53.5	28.8
161	-52.3	28.8
209	-52.2	28.8
193	-52.0	28.9
241	-51.4	28.9
233	-50.5	29.0
193	-51.5	29.0
209	-51.4	29.0
273	-48.9	29.0
161	-47.5	29.1
193	-49.8	29.1
201_I	-52.7	29.1
233	-54.7	29.1
281	-55.2	29.2
313	-53.3	29.3
257_I	-53.5	29.3
305	-50.5	29.3
169	-53.3	29.4
297	-51.5	29.4

Experimental Run 1A raw coal percentage and aspect ratio data:

Phase One:

Count	Area	Size	StdDev	Major	Minor	Maj/Min
1	1.2	5.0	6.5	3.4	0.4	7.8
2	0.1	0.5	7.0	0.6	0.3	1.9
3	1.0	4.0	5.5	2.9	0.4	6.7
4	1.1	4.5	5.6	3.4	0.4	8.4
5	0.2	0.9	7.2	1.0	0.3	3.8
6	0.8	3.5	6.4	3.0	0.4	8.6
7	0.3	1.1	7.9	2.3	0.1	16.0
8	1.5	6.3	5.9	5.3	0.4	14.5
9	1.5	6.3	6.5	4.4	0.4	10.0
10	0.03	0.1	10.0	0.2	0.1	1.7

Phase Two:

Count	Area	Size	StdDev	Major	Minor	Maj/Min
1	0.4	1.6	7.6	2.4	0.2	12.1
2	0.3	1.5	7.9	2.2	0.2	11.9
3	0.1	0.4	9.5	0.7	0.2	3.9
4	0.1	0.4	8.9	0.7	0.2	4.6
5	0.6	2.6	6.8	2.9	0.3	11.5
6	0.1	0.6	9.0	0.8	0.2	4.5
7	0.04	0.2	9.6	0.5	0.1	5.4
8	0.1	0.3	10.8	0.6	0.1	4.3
9	0.2	0.7	8.1	1.0	0.2	5.1
10	0.7	3.0	6.3	2.6	0.3	7.9
11	0.5	2.2	5.9	1.6	0.4	4.1
12	0.2	1.0	7.5	1.1	0.3	4.1
13	0.3	1.4	8.5	1.8	0.2	8.1
14	0.3	1.3	8.0	1.8	0.2	8.6
15	0.3	1.3	7.5	1.7	0.2	7.7
16	0.4	2.0	7.8	1.6	0.3	4.7
17	0.2	0.7	8.2	1.2	0.2	6.6
18	0.3	1.4	8.1	1.7	0.2	7.4
19	0.1	0.3	9.2	0.7	0.1	4.5
20	0.6	2.7	5.6	1.7	0.4	4.0

Phase Three:

Count	Area	Size	StdDev	Major	Minor	Maj/Min
1	0.4	2.0	6.3	2.1	0.2	8.8
2	0.2	1.1	7.0	1.0	0.3	3.7
3	0.6	3.0	6.2	2.1	0.4	5.9
4	0.5	2.2	8.3	1.8	0.3	5.4
5	0.6	3.0	6.6	3.0	0.3	11.9
6	0.1	0.6	8.6	0.8	0.2	3.7
7	0.03	0.1	8.3	0.3	0.1	2.3
8	0.2	0.8	7.7	1.0	0.2	5.5
9	0.1	0.4	9.7	0.6	0.2	3.5
10	0.4	1.7	7.2	2.1	0.2	9.5
11	0.6	3.0	6.7	3.3	0.2	14.2
12	0.2	0.9	8.2	1.0	0.2	4.2
13	0.3	1.3	8.6	1.7	0.2	8.9
14	0.3	1.3	8.1	1.9	0.2	10.5
15	0.2	1.0	9.0	1.4	0.2	7.6

Phase Four:

Count	Area	Size	StdDev	Major	Minor	Maj/Min
1	0.1	1.1	17.4	1.0	0.1	7.2
2	0.04	0.4	17.2	0.4	0.1	3.0
3	0.1	0.7	14.8	0.6	0.2	3.8
4	0.04	0.4	19.9	0.4	0.1	3.2
5	0.05	0.5	18.8	0.3	0.2	1.9
6	0.2	1.5	15.5	1.3	0.2	8.2
7	0.02	0.2	20.0	0.2	0.1	1.8
8	0.05	0.5	16.3	0.4	0.2	2.5
9	0.05	0.5	19.8	0.5	0.1	3.8
10	0.03	0.3	17.6	0.3	0.1	2.4

Phase Five:

Count	Area	Size	StdDev	Major	Minor	Maj/Min
1	0.1	0.7	10.2	0.5	0.3	1.8
2	0.5	3.3	7.6	2.8	0.2	11.7
3	0.1	0.9	8.6	0.6	0.3	2.1
4	2.4	14.8	7.0	2.9	1.1	2.7
5	0.3	2.0	9.4	1.3	0.3	3.9
6	0.3	1.9	7.8	1.4	0.3	4.7
7	0.1	0.3	9.5	0.4	0.1	2.9
8	0.1	0.7	8.6	0.7	0.2	3.7
9	0.3	1.7	6.6	1.1	0.3	3.6
10	0.03	0.2	10.1	0.3	0.2	1.6
11	0.1	0.8	9.5	1.2	0.1	8.6
12	0.04	0.2	11.3	0.5	0.1	5.5
13	0.2	1.5	7.0	1.2	0.3	4.6

Experimental Run 1B raw coal percentage and aspect ratio data:

Phase One:

Count	Area	Size	StdDev	Major	Minor	Maj/Min
1	0.2	1.5	7.8	1.3	0.2	6.1
2	0.8	5.8	6.9	3.8	0.3	13.8
3	0.3	1.8	9.0	2.1	0.2	13.8
4	0.1	0.4	12.3	0.7	0.1	6.3
5	1.3	9.3	7.1	4.1	0.4	9.6
6	0.6	4.2	8.8	1.9	0.4	4.9
7	0.3	2.0	12.4	0.9	0.4	2.2
8	0.1	0.5	12.7	0.5	0.2	3.2
9	0.1	0.7	9.3	0.6	0.2	2.7
10	0.05	0.3	11.8	0.4	0.1	3.3
11	0.02	0.1	13.7	0.2	0.1	1.7
12	0.02	0.1	14.6	0.2	0.1	1.4
13	0.04	0.3	11.6	0.4	0.1	2.5

Phase Two:

Count	Area	Size	StdDev	Major	Minor	Maj/Min
1	0.3	1.6	6.3	1.7	0.2	8.2
2	0.3	1.9	6.3	2.2	0.2	11.3
3	0.03	0.2	8.9	0.4	0.1	3.9
4	0.2	1.4	6.2	1.8	0.2	10.3
5	0.04	0.2	7.8	0.3	0.1	2.5
6	0.2	1.2	6.5	1.4	0.2	7.0
7	0.3	1.5	5.9	1.6	0.2	7.7
8	0.3	1.9	5.4	1.8	0.2	7.3
9	0.04	0.2	7.1	0.3	0.2	2.1
10	0.3	1.6	5.8	1.3	0.3	4.4
11	0.1	0.8	6.2	0.8	0.2	3.8
12	0.03	0.1	7.8	0.4	0.1	4.3
13	0.2	1.0	6.7	1.4	0.2	8.4
14	0.1	0.4	6.6	0.4	0.2	2.1
15	0.2	1.2	6.8	0.7	0.4	1.9
16	0.1	0.5	7.1	0.8	0.2	5.1
17	0.1	0.3	8.1	0.4	0.2	2.2
18	0.3	1.4	5.6	1.1	0.3	3.8

Phase Three:

Count	Area	Size	StdDev	Major	Minor	Maj/Min
1	1.2	4.2	6.6	3.6	0.4	8.4
2	0.3	1.0	7.4	1.7	0.2	8.3
3	0.4	1.2	7.2	2.3	0.2	12.2
4	2.7	9.5	5.9	4.5	0.8	5.8
5	0.03	0.1	7.4	0.3	0.1	2.6
6	0.1	0.4	8.6	1.2	0.1	11.0
7	0.7	2.6	6.7	1.7	0.6	3.1
8	0.1	0.2	7.6	0.4	0.2	2.1
9	0.1	0.3	7.6	0.7	0.2	4.4
10	0.1	0.4	7.2	0.8	0.2	4.5
11	0.1	0.3	7.1	0.7	0.1	4.8
12	0.1	0.3	6.9	0.6	0.2	3.4
13	0.1	0.2	10.4	0.3	0.2	1.4
14	0.04	0.1	10.8	0.5	0.1	3.8
15	0.02	0.1	8.4	0.2	0.1	1.6
16	0.04	0.1	8.6	0.4	0.1	3.8
17	0.2	0.6	6.8	1.1	0.2	5.6
18	0.2	0.8	6.5	1.4	0.2	7.3
19	0.02	0.1	10.1	0.2	0.1	1.4
20	0.3	0.9	7.6	2.3	0.1	15.7
21	0.1	0.2	9.8	0.7	0.1	7.0

Phase Four:

Count	Area	Size	StdDev	Major	Minor	Maj/Min
1	0.2	1.1	6.3	1.3	0.2	7.2
2	1.4	8.1	5.7	4.2	0.4	9.8
3	0.04	0.2	7.9	0.4	0.2	2.2
4	0.01	0.1	11.9	0.1	0.1	1.8
5	0.1	0.3	8.2	0.5	0.1	3.3
6	0.01	0.0	13.1	0.1	0.1	1.5
7	0.1	0.4	8.2	0.6	0.1	5.0
8	0.1	0.6	9.5	1.0	0.1	8.0
9	0.1	0.7	6.4	0.9	0.2	5.0
10	0.3	1.8	7.3	2.0	0.2	10.1
11	0.1	0.4	8.3	0.5	0.2	3.4
12	0.1	0.5	7.6	0.6	0.2	3.8
13	0.02	0.1	8.1	0.2	0.1	1.6
14	0.1	0.4	6.6	0.4	0.3	1.3
15	0.1	0.6	7.8	1.3	0.1	11.2
16	0.3	1.8	6.6	1.7	0.2	7.5
17	0.1	0.6	9.1	0.9	0.2	5.4
18	0.04	0.2	6.5	0.3	0.2	1.4
19	0.4	2.4	6.4	1.8	0.3	5.9
20	0.1	0.3	7.9	0.5	0.1	4.6
21	0.04	0.2	7.4	0.3	0.2	1.7

Phase Five:

Count	Area	Size	StdDev	Major	Minor	Maj/Min
1	0.1	0.7	10.2	0.5	0.3	1.8
2	0.5	3.3	7.6	2.8	0.2	11.7
3	0.1	0.9	8.6	0.6	0.3	2.1
4	2.4	14.8	7.0	2.9	1.1	2.7
5	0.3	2.0	9.4	1.3	0.3	3.9
6	0.3	1.9	7.8	1.4	0.3	4.7
7	0.1	0.3	9.5	0.4	0.1	2.9
8	0.1	0.7	8.6	0.7	0.2	3.7
9	0.3	1.7	6.6	1.1	0.3	3.6
10	0.03	0.2	10.1	0.3	0.2	1.6
11	0.1	0.8	9.5	1.2	0.1	8.6
12	0.04	0.2	11.3	0.5	0.1	5.5
13	0.2	1.5	7.0	1.2	0.3	4.6

Experimental Run 1C raw coal percentage and aspect ratio data:

Phase One:

Count	Area	Size	StdDev	Major	Minor	Maj/Min
1	0.3	5.8	15.9	0.9	0.4	2.5
2	0.05	1.1	19.7	0.3	0.2	1.6
3	0.3	5.7	14.0	0.9	0.3	2.7
4	0.04	0.8	16.9	0.3	0.2	1.6
5	0.01	0.2	25.2	0.1	0.1	1.4
6	0.01	0.3	22.4	0.2	0.1	2.1
7	0.01	0.2	25.0	0.1	0.1	1.5
8	0.1	1.4	20.4	0.4	0.2	2.5
9	0.2	4.6	16.7	1.4	0.2	7.8
10	0.1	1.7	18.2	0.5	0.2	3.0
11	0.1	1.8	15.2	0.5	0.2	2.8
12	0.1	2.6	15.0	0.8	0.2	4.2
13	0.01	0.3	18.9	0.2	0.1	2.0
14	0.2	3.9	12.9	1.1	0.2	5.3
15	0.01	0.2	24.3	0.1	0.1	1.5
16	0.02	0.5	27.7	0.2	0.1	2.1
17	0.01	0.2	26.0	0.1	0.1	2.3

Phase Two:

Count	Area	Size	StdDev	Major	Minor	Maj/Min
1	0.2	1.0	9.5	1.4	0.2	9.3
2	0.03	0.1	13.5	0.3	0.1	3.0
3	0.3	1.5	9.9	1.9	0.2	10.6
4	0.05	0.3	11.5	0.4	0.1	3.0
5	0.02	0.1	10.7	0.2	0.1	1.7
6	0.01	0.1	14.0	0.2	0.1	1.5
7	0.02	0.1	11.7	0.2	0.1	1.6
8	2.6	14.5	8.0	2.7	1.2	2.2
9	0.1	0.6	11.1	0.5	0.3	2.0
10	0.4	2.2	7.8	1.6	0.3	5.4
11	0.2	0.9	7.9	0.5	0.4	1.3
12	0.02	0.1	11.4	0.3	0.1	2.4
13	1.5	8.4	7.8	2.5	0.8	3.2
14	0.02	0.1	12.9	0.3	0.1	2.8
15	0.04	0.2	10.1	0.3	0.1	2.4
16	0.01	0.03	15.6	0.1	0.1	1.1

Phase Three:

Count	Area	Size	StdDev	Major	Minor	Maj/Min
1	0.1	0.6	8.0	0.8	0.2	4.2
2	1.2	6.1	7.0	3.9	0.4	10.2
3	0.6	2.9	7.7	1.7	0.4	4.1
4	0.03	0.2	11.0	0.4	0.1	4.2
5	0.02	0.1	11.6	0.3	0.1	3.2
6	0.8	4.2	7.5	2.3	0.4	5.4
7	0.01	0.1	10.8	0.2	0.1	2.7
8	0.1	0.4	9.5	0.7	0.2	4.6
9	0.03	0.2	13.1	0.2	0.2	1.1
10	0.03	0.1	11.2	0.3	0.1	3.5
11	0.02	0.1	11.6	0.2	0.1	2.3
12	0.1	0.5	9.3	0.8	0.2	4.7
13	0.3	1.3	7.4	1.3	0.2	5.3
14	1.1	5.8	8.6	2.2	0.7	3.3
15	0.1	0.4	9.0	0.9	0.1	7.0
16	0.1	0.6	7.1	0.5	0.3	1.9
17	0.04	0.2	10.2	0.4	0.1	3.1
18	0.2	1.0	7.4	1.0	0.2	3.9
19	0.03	0.2	12.1	0.3	0.1	2.8
20	0.1	0.3	12.2	0.6	0.1	4.9
21	0.1	0.4	8.8	0.5	0.2	2.0
22	0.1	0.4	10.5	0.7	0.1	6.1
23	0.2	1.1	8.7	0.7	0.4	1.6
24	0.01	0.1	13.2	0.2	0.1	2.9

Phase Four:

Count	Area	Size	StdDev	Major	Minor	Maj/Min
1	0.8	9.2	9.5	1.6	0.6	2.5
2	0.4	4.8	7.9	1.7	0.3	5.5
3	1.0	12.0	8.5	2.2	0.6	3.5
4	0.04	0.5	9.9	0.4	0.1	2.4
5	0.1	0.7	12.3	0.7	0.1	5.9
6	0.1	1.4	9.8	0.6	0.3	2.3
7	0.3	3.0	9.0	1.4	0.2	6.2
8	0.02	0.3	14.3	0.3	0.1	3.5
9	0.04	0.4	15.0	0.6	0.1	8.7

Phase Five:

Count	Area	Size	StdDev	Major	Minor	Maj/Min
1	1.8	17.2	7.3	2.6	0.9	3.0
2	0.1	0.7	11.2	0.6	0.1	4.1
3	0.05	0.5	8.5	0.3	0.2	1.2
4	0.02	0.2	11.1	0.3	0.1	2.9
5	0.02	0.2	11.6	0.2	0.1	1.6
6	0.03	0.3	12.3	0.4	0.1	5.3
7	0.01	0.1	12.8	0.2	0.1	2.2
8	0.02	0.2	13.4	0.2	0.1	2.4
9	0.1	0.5	11.0	0.6	0.1	5.5
10	0.1	0.6	10.9	0.8	0.1	8.6
11	0.04	0.4	10.5	0.3	0.1	2.4
12	0.1	1.4	9.2	1.2	0.1	8.4
13	0.02	0.2	12.1	0.3	0.1	3.3
14	0.02	0.2	11.8	0.3	0.1	3.6
15	0.01	0.1	11.1	0.1	0.1	1.6
16	0.4	3.6	8.9	1.2	0.4	3.1
17	0.01	0.1	11.9	0.2	0.1	2.0
18	0.1	0.6	7.6	0.5	0.2	2.6
19	0.03	0.3	9.3	0.2	0.2	1.1
20	0.02	0.2	11.8	0.2	0.1	1.6
21	0.04	0.4	13.2	0.7	0.1	9.4

Experimental Run 2A raw coal percentage and aspect ratio data:

Phase One:

Count	Area	Size	StdDev	Major	Minor	Maj/Min
1	0.2	2.0	10.1	1.3	0.2	7.5
2	0.04	0.5	10.9	0.4	0.1	3.3
3	0.1	0.8	9.0	0.7	0.1	5.5
4	0.1	0.8	10.6	1.0	0.1	11.9
5	0.1	0.6	8.8	0.5	0.1	3.6
6	0.1	0.6	10.5	0.8	0.1	9.5
7	0.05	0.5	9.5	0.4	0.2	2.4
8	0.04	0.4	12.8	0.6	0.1	7.0
9	0.03	0.3	12.3	0.3	0.1	1.9
10	0.1	0.6	12.3	0.8	0.1	9.3
11	0.04	0.5	12.5	0.5	0.1	4.4
12	0.02	0.2	10.3	0.2	0.1	2.1
13	0.02	0.2	10.8	0.2	0.1	2.0
14	0.2	2.5	9.8	1.4	0.2	7.1
15	0.2	2.6	7.5	1.4	0.2	6.3
16	0.2	1.8	8.0	1.2	0.2	7.1
17	0.02	0.2	12.1	0.2	0.1	2.4

Phase Two:

Count	Area	Size	StdDev	Major	Minor	Maj/Min
1	0.1	0.9	9.4	0.7	0.2	3.5
2	0.2	1.3	10.7	1.7	0.1	14.6
3	0.4	3.0	7.8	1.9	0.2	7.9
4	0.8	6.1	7.3	1.7	0.6	2.8
5	0.03	0.3	11.6	0.4	0.1	4.3
6	0.02	0.2	13.4	0.3	0.1	2.5
7	0.4	3.2	9.1	2.1	0.2	8.6
8	0.3	2.7	8.7	1.1	0.4	2.8
9	0.1	0.9	7.8	0.7	0.2	3.3
10	0.3	2.2	9.4	2.7	0.1	20.7
11	0.1	0.6	9.1	0.7	0.1	5.4
12	0.2	1.6	8.6	1.2	0.2	5.8
13	0.01	0.0	13.8	0.1	0.1	1.4
14	0.1	1.1	8.0	0.8	0.2	3.8
15	0.1	0.5	9.9	0.6	0.1	5.4
16	0.2	1.8	7.6	1.6	0.2	8.7
17	0.03	0.3	10.3	0.3	0.1	2.6

Phase Three:

Count	Area	Size	StdDev	Major	Minor	Maj/Min
1	1.6	6.4	8.3	5.4	0.4	14.0
2	0.02	0.1	11.7	0.3	0.1	2.8
3	0.05	0.2	11.9	0.6	0.1	5.2
4	0.1	0.4	10.2	0.8	0.2	4.8
5	0.02	0.1	11.6	0.2	0.1	1.8
6	0.1	0.3	11.3	0.8	0.1	8.2
7	1.3	5.1	7.9	2.2	0.8	2.8
8	0.04	0.2	12.8	0.6	0.1	5.5
9	0.6	2.4	7.2	3.0	0.3	11.1
10	0.2	0.7	10.1	1.3	0.2	7.7
11	0.02	0.1	12.4	0.4	0.1	4.4
12	0.05	0.2	10.4	0.4	0.1	2.7
13	0.6	2.3	7.9	2.2	0.3	6.5
14	0.5	1.8	7.3	1.0	0.6	1.7
15	0.04	0.2	10.1	0.4	0.1	2.8
16	0.1	0.2	10.6	0.6	0.1	5.3
17	0.1	0.2	9.7	0.6	0.1	4.6
18	0.4	1.4	5.9	1.4	0.3	4.2
19	0.1	0.5	9.9	1.1	0.1	8.1
20	0.1	0.4	10.3	0.6	0.2	2.7
21	0.3	1.1	10.3	2.0	0.2	10.8
22	0.02	0.1	11.8	0.3	0.1	2.6
23	0.1	0.3	9.8	0.6	0.2	3.9
24	0.1	0.4	9.5	0.7	0.2	3.3
25	0.5	2.0	8.1	3.0	0.2	14.1
26	0.1	0.4	10.1	1.1	0.1	7.9

Phase Four:

Count	Area	Size	StdDev	Major	Minor	Maj/Min
1	0.04	0.7	11.0	0.5	0.1	4.5
2	0.04	0.7	10.6	0.4	0.1	3.4
3	0.1	2.7	8.4	0.6	0.3	1.8
4	0.8	16.0	7.5	2.5	0.4	5.9
5	0.3	6.7	8.4	1.6	0.3	5.4
6	0.1	1.1	10.6	0.5	0.1	4.2
7	0.03	0.5	9.6	0.3	0.1	2.1

Phase Five:

Count	Area	Size	StdDev	Major	Minor	Maj/Min
1	0.04	1.0	10.2	0.5	0.1	4.3
2	1.4	32.0	8.4	4.0	0.4	9.1
3	0.04	0.8	9.4	0.4	0.1	4.2
4	0.1	1.3	10.3	0.4	0.2	2.4
5	0.03	0.7	10.0	0.5	0.1	5.7
6	0.1	2.0	10.1	0.6	0.2	2.8
7	0.03	0.7	10.4	0.2	0.2	1.3

Experimental Run 2B raw coal percentage and aspect ratio data:

Phase One:

Count	Area	Size	StdDev	Major	Minor	Maj/Min
1	0.1	1.8	8.5	0.7	0.2	4.6
2	0.05	0.9	9.6	0.5	0.1	4.4
3	0.4	7.9	8.4	1.4	0.4	3.5
4	0.2	4.0	9.2	2.1	0.1	16.7
5	0.2	4.5	6.9	1.0	0.3	3.4
6	0.1	1.4	11.4	0.6	0.2	4.3
7	0.1	1.5	8.1	0.4	0.3	1.5
8	0.1	2.5	9.5	0.7	0.2	2.8
9	0.1	1.2	10.0	0.6	0.1	5.0
10	0.1	1.3	9.8	0.6	0.2	3.5
11	0.03	0.6	10.4	0.4	0.1	3.9

Phase Two:

Count	Area	Size	StdDev	Major	Minor	Maj/Min
1	0.02	0.3	13.2	0.4	0.1	6.6
2	0.1	1.2	10.4	0.9	0.1	6.8
3	0.03	0.3	11.8	0.4	0.1	4.3
4	0.02	0.2	11.8	0.3	0.1	2.7
5	0.2	2.0	10.7	1.6	0.1	13.5
6	0.1	1.4	10.4	1.3	0.1	12.3
7	0.1	0.9	9.7	0.7	0.1	5.9
8	0.03	0.4	11.7	0.5	0.1	5.7
9	0.02	0.3	8.8	0.2	0.2	1.2
10	0.2	2.2	9.8	1.6	0.1	11.4
11	0.1	1.9	9.7	1.3	0.1	8.7
12	0.1	1.0	10.2	0.7	0.1	5.3

Phase Three:

Count	Area	Size	StdDev	Major	Minor	Maj/Min
1	0.3	1.6	7.6	1.4	0.3	4.8
2	0.4	2.2	7.3	2.4	0.2	10.0
3	0.5	2.3	6.3	1.7	0.3	5.2
4	0.04	0.2	10.3	0.4	0.1	3.7
5	0.02	0.1	12.0	0.3	0.1	3.3
6	0.05	0.2	9.9	0.6	0.1	7.0
7	0.2	0.8	9.2	1.8	0.1	15.8
8	0.1	0.7	10.2	0.7	0.3	2.6
9	0.1	0.7	9.6	1.3	0.1	9.7
10	0.1	0.6	10.8	1.3	0.1	11.5
11	0.1	0.6	10.2	1.2	0.1	8.6
12	0.05	0.2	10.6	0.6	0.1	6.6
13	0.03	0.2	11.0	0.5	0.1	7.0
14	0.02	0.1	9.7	0.3	0.1	4.3
15	0.03	0.1	11.0	0.4	0.1	3.8
16	0.2	0.8	8.9	1.1	0.2	6.6
17	0.05	0.2	12.3	0.9	0.1	14.0
18	0.04	0.2	14.1	0.7	0.1	10.4
19	0.1	0.4	11.4	0.9	0.1	8.1
20	0.3	1.3	8.5	1.0	0.4	2.7
21	0.2	1.0	6.7	1.1	0.2	4.6
22	0.2	0.9	9.7	1.4	0.2	8.7
23	0.02	0.1	11.2	0.3	0.1	2.5
24	0.1	0.3	11.2	0.8	0.1	7.8
25	0.1	0.3	9.1	0.7	0.1	5.8
26	0.1	0.4	8.9	0.7	0.1	5.5
27	0.1	0.7	8.8	1.2	0.2	7.3
28	0.1	0.3	9.6	0.7	0.1	5.4

Phase Four:

Count	Area	Size	StdDev	Major	Minor	Maj/Min
1	0.1	1.2	9.8	0.9	0.1	6.2
2	0.1	1.2	9.0	0.9	0.1	6.3
3	0.1	0.8	10.5	0.7	0.1	6.5
4	0.03	0.4	12.3	0.5	0.1	5.3
5	0.02	0.3	11.7	0.3	0.1	2.6
6	0.02	0.3	11.1	0.2	0.1	2.1
7	0.1	0.6	10.5	0.6	0.1	4.9
8	0.02	0.2	10.3	0.3	0.1	2.8
9	0.02	0.3	12.4	0.3	0.1	4.3
10	0.1	0.6	12.0	0.6	0.1	5.6
11	0.03	0.3	10.5	0.3	0.1	2.8
12	0.05	0.6	10.9	0.5	0.1	4.3
13	0.1	0.9	9.9	0.6	0.2	3.9
14	0.03	0.3	11.7	0.3	0.1	2.9
15	0.01	0.2	12.7	0.2	0.1	2.3
16	0.03	0.4	11.1	0.3	0.1	2.2
17	0.04	0.5	11.3	0.5	0.1	4.4
18	0.2	1.9	8.7	1.4	0.1	10.5
19	0.02	0.2	9.7	0.2	0.1	2.8
20	0.04	0.4	10.0	0.3	0.2	1.9
21	0.1	0.8	10.2	0.6	0.1	4.8
22	0.03	0.3	12.8	0.4	0.1	4.1
23	0.2	2.7	8.9	1.0	0.3	3.2
24	0.1	0.7	11.5	0.8	0.1	7.8
25	0.1	0.8	10.2	0.6	0.1	4.3

Phase Five:

Count	Area	Size	StdDev	Major	Minor	Maj/Min
1	0.02	0.3	12.0	0.3	0.1	2.7
2	0.02	0.4	11.2	0.3	0.1	3.7
3	0.02	0.3	14.7	0.4	0.1	6.9
4	0.04	0.6	10.4	0.4	0.1	2.9
5	0.1	1.3	10.7	1.0	0.1	8.9
6	0.1	1.6	9.6	0.6	0.2	2.5
7	0.02	0.4	10.6	0.3	0.1	2.4
8	0.2	3.6	7.8	1.5	0.2	7.6
9	0.02	0.4	13.0	0.4	0.1	4.4
10	0.1	1.0	10.6	0.6	0.1	4.4
11	0.1	1.2	9.9	0.5	0.2	2.3
12	0.03	0.5	12.4	0.4	0.1	3.9
13	0.02	0.3	14.2	0.3	0.1	4.3
14	0.1	1.7	9.0	0.9	0.1	6.3
15	0.1	0.9	10.2	0.5	0.1	4.2
16	0.1	1.4	8.2	0.6	0.2	3.2
17	0.05	0.7	11.2	0.4	0.1	3.4
18	0.04	0.6	10.1	0.4	0.1	3.9
19	0.1	1.4	9.5	0.6	0.2	2.9
20	0.03	0.5	11.0	0.4	0.1	3.7
21	0.03	0.5	10.6	0.4	0.1	4.1